J. Fluid Mech. (2021), *vol*. 918, A40, doi:10.1017/jfm.2021.236

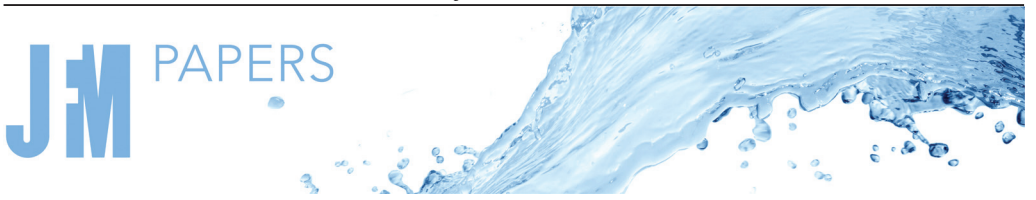

Contributions of different scales of turbulent motions to the mean wall-shear stress in open channel flows at low-to-moderate Reynolds numbers

Yanchong Duan[1], Qiang Zhong[2,3,†], Guiquan Wang[4], Peng Zhang[5] and Danxun Li[1]

[1]State Key Laboratory of Hydroscience and Engineering, Tsinghua University, Beijing 100084, PR China

[2]College of Water Resources and Civil Engineering, China Agricultural University, Beijing 100083, PR China

[3]Beijing Engineering Research Center of Safety and Energy Saving Technology for Water Supply Network System, China Agricultural University, Beijing 100083, PR China

[4]Physics of Fluids Group and Twente Max Planck Center, Department of Science and Technology, Mesa+ Institute, and J.M. Burgers Center for Fluid Dynamics, University of Twente, P.O. Box 217, Enschede 7500 AE, The Netherlands

[5]National Engineering Research Center for Inland Waterway Regulation, Chongqing Jiaotong University, Chongqing 400074, PR China

(Received 2 September 2020; revised 1 February 2021; accepted 12 March 2021)

Smooth-walled open channel flow datasets, covering both the direct numerical simulation and experimental measurements with a friction Reynolds number Re_τ at a low-to-moderate level of $550 \sim 2400$, are adopted to investigate the contributions of different scale motions to the mean wall-shear stress in open channel flows (OCFs). The FIK identity decomposition method by Fukagata *et al.* (*Phys. Fluids*, vol. 14, 2002, L73) combined with a scale decomposition is chosen for this research. To see whether/how the contributions in OCFs differ with those in closed channel flows (CCFs), comparisons between the two flows are also made. The scale-decomposed 'turbulent' contribution results of present OCFs exhibit two dominant contribution modes (i.e. large-scale motions (LSMs) and very-large-scale motions (VLSMs)) at a streamwise wavelength $\lambda_x = 1 \sim 2h$ and $O(10h)$, where h is the water depth. The large scales with $\lambda_x > 3h$ and $\lambda_x > 10h$ are demonstrated to contribute to over 40 % and 20 % of the mean wall-shear stress, respectively. Compared with CCFs, slightly higher and lower contributions in the $\lambda_x > O(10h)$ and $\lambda_x < O(10h)$ wavelength ranges are observed in OCFs, revealing the important free-surface effects in

† Email address for correspondence: qzhong@cau.edu.cn

OCFs. Possible mechanisms are discussed to lend support for the observed differences between the two flows.

Key words: turbulent boundary layers, channel flow

1. Introduction

The wall-shear stress, τ_w, is of interest for wall-bounded turbulent flows. Its time-averaged value $\langle\tau_w\rangle$ (i.e. the mean wall-shear stress), in particular, has fundamental and practical importance. On the one hand, $\langle\tau_w\rangle$ provides key scaling parameters for theoretical treatment of wall-bounded turbulent flows, i.e. the friction velocity $u_\tau = \sqrt{\langle\tau_w\rangle/\rho}$ as the inner velocity scale and $l^* = \nu/u_\tau$ as the inner length scale (here ρ is fluid density and ν is kinematic viscosity). On the other hand, $\langle\tau_w\rangle$ not only accounts for a major portion of the total drag in various wall turbulence applications (e.g. 50 % for aircraft, 90 % for submarine, etc. Gad-el-Hak 1994; Fan, Cheng & Li 2019*a*; Li *et al.* 2019), but also exhibits close relevance to wall surface morphology (such as bed load transport in rivers, wind-blown sand movement in desert, etc.).

Given the essential significance, sustained research efforts have been made to determine $\langle\tau_w\rangle$ (Winter 1979; Haritonidis 1989; Klewicki *et al.* 2007; Walker 2014; Cierpka, Rossi & Köhler 2015; Rathakrishnan 2017; Vinuesa & Örlü 2017, etc.) and to clarify its generation mechanism. Although $\langle\tau_w\rangle$ is a wall quantity that can be directly calculated from the wall-normal gradient of the mean streamwise velocity, its generation involves flow dynamics across the whole wall layer. Accordingly, a thorough understanding of $\langle\tau_w\rangle$ requires an appropriate expression connecting $\langle\tau_w\rangle$ to turbulent characteristics across the whole flow.

A typical expression has been proposed by Fukagata, Iwamoto & Kasagi (2002) based on a triple integration to the Reynolds averaged Navier–Stokes equation. The analytical expression, often referred to as the FIK identity, relates the friction coefficient C_f (which can be regarded as a dimensionless representation of $\langle\tau_w\rangle$) to the Reynolds shear stress distribution. In Fukagata *et al.* (2002), the expressions for three canonical wall-bounded turbulent flows (i.e. closed channel flow (CCF), pipe flow (PF), and turbulent boundary layer (TBL)) have been derived, according to which C_f can be decomposed into three components, i.e. laminar, turbulent and streamwise inhomogenous components (see the TBL flow scenario). Regarding the CCF (as well as the open channel flow (OCF)) scenario considered herein where the inhomogenous component is absent, the FIK identity can be expressed as follows:

$$C_f = \underbrace{\frac{6}{Re_b}}_{C_{f1,FIK}} + \underbrace{6\int_0^1 \left(1-\frac{y}{h}\right)\left(\frac{-\langle uv\rangle}{U_b^2}\right)\mathrm{d}\left(\frac{y}{h}\right)}_{C_{f2,FIK}}, \tag{1.1}$$

where $C_f = 2\langle\tau_w\rangle/(\rho U_b^2)$ with U_b as the bulk velocity, $Re_b = U_b h/\nu$ is the bulk Reynolds number (h, channel half-height for CCF and water depth for OCF), y is the wall-normal distance to the wall and $-\langle uv\rangle$ is the Reynolds shear stress. The FIK identity in (1.1) is generally interpreted as a physical decomposition of $\langle\tau_w\rangle$ according to its generation mechanism: the first term $C_{f1,FIK}$ is the so-called 'laminar' contribution given its similarity to laminar flow cases, while the second term $C_{f2,FIK}$ represents the 'turbulent' contribution quantified through the linearly weighted integral of the Reynolds shear stress.

Since its proposition, the FIK identity has drawn a large amount of attention, and many modifications/extensions have been proposed to expand its applicability in more diverse flow cases. The applications of FIK identity (and its modified/extended versions) can be seen in various wall turbulence scenarios, e.g. CCFs (Iwamoto *et al.* 2005; Stroh *et al.* 2015; de Giovanetti, Hwang & Choi 2016; Agostini & Leschziner 2019; Cheng *et al.* 2019; Fan *et al.* 2019*a*), zero/adverse pressure gradient TBLs (Kametani & Fukagata 2011; Mehdi & White 2011; Deck *et al.* 2014; Mehdi *et al.* 2014; Kametani *et al.* 2015; Stroh *et al.* 2015; Senthil *et al.* 2020), fully three-dimensional flow over walls of complex geometry (Peet & Sagaut 2009; Bannier, Garnier & Sagaut 2015), compressible CCFs (Gomez, Flutet & Sagaut 2009), viscoelastic CCFs (Zhang *et al.* 2020), square duct flows (Modesti *et al.* 2018) and rough-walled OCFs (Kuwata & Kawaguchi 2018; Nikora *et al.* 2019).

In addition to the FIK identity, other decomposition methods have also emerged in the last few years. For instance, Renard & Deck (2016) proposed an alternative method (usually referred to as the RD identity) from the mean streamwise kinetic-energy budget. Similar to the FIK identity, there are also three decomposed components in the RD identity for the TBL flow scenario with the third component also representing the inhomogeneity of the flow. In terms of the CCF as well as OCF flow scenarios, since the third component is zero, the RD identity can be expressed as

$$C_f = \underbrace{\frac{2h}{U_b^3}\int_0^1 \nu\left(\frac{\partial U}{\partial y}\right)^2 \mathrm{d}\left(\frac{y}{h}\right)}_{C_{f1,RD}} + \underbrace{\frac{2h}{U_b^3}\int_0^1 (-\langle uv\rangle)\frac{\partial U}{\partial y}\mathrm{d}\left(\frac{y}{h}\right)}_{C_{f2,RD}}, \tag{1.2}$$

where $\partial U/\partial y$ is the wall-normal gradient of the mean streamwise velocity U. In physics, the RD identity decomposes $\langle\tau_w\rangle$ from the power perspective, i.e. treating the power of $\langle\tau_w\rangle$ as an energy transfer from the wall to the fluid through viscous dissipation ($C_{f1,RD}$) and turbulent kinetic energy (TKE) production ($C_{f2,RD}$). The RD identity as well as its modifications/extensions have also been widely used: CCFs (Agostini & Leschziner 2019; Fan *et al.* 2019*a*); zero/adverse pressure gradient TBLs (Renard & Deck 2016, 2017; Fan, Li & Pirozzoli 2019*b*; Senthil *et al.* 2020); compressible CCFs (Li *et al.* 2019); compressible TBLs (Fan *et al.* 2019*b*); viscoelastic CCFs (Zhang *et al.* 2020), etc.

Almost at the same time that the RD identity was proposed, Yoon *et al.* (2016) presented another decomposition method. This method relates $\langle\tau_w\rangle$ to the vortical motions by integrating the mean vorticity equation, and decomposes C_f into contributions from advective vorticity transport, vortex stretching, viscous and inhomogeneous terms. Some applications of this method can be found in subsequent studies of zero/adverse pressure gradient TBLs (Hwang & Sung 2017; Kim *et al.* 2017; Yoon, Hwang & Sung 2018).

The three decomposition methods are all physically sound and have their own unique features given that they decompose $\langle\tau_w\rangle$ from different perspectives. Accordingly, the obtained results differ from each other, and the method chosen in a specific study generally depends on the research purpose.

As seen in the review above, in contrast to abundant research in CCFs and TBLs, only a few studies have paid attention to OCFs. Recently, Kuwata & Kawaguchi (2018) used the FIK identity to decompose C_f into five components (laminar, turbulence, dispersion, drag and inhomogeneous correction) in rough-walled OCFs with wall surface randomly covered by semi-spheres. In rough-walled OCFs with more general wall conditions, Nikora *et al.* (2019) extended the FIK identity and proposed a theoretical decomposition of the Darcy–Weisbach friction factor f (equivalent to $4C_f$), based on which C_f can be decomposed into four components (viscous, turbulence, dispersive

and inertial, three-dimensionality, and non-uniformity). Though the work by Kuwata & Kawaguchi (2018) and Nikora *et al.* (2019) advanced our understandings of $\langle\tau_w\rangle$ generation in (rough-walled) OCFs, many important issues are yet to be clarified.

Firstly, since only the overall contributions of each decomposed component were quantified in Kuwata & Kawaguchi (2018) and Nikora *et al.* (2019) for (rough-walled) OCFs, it is still unclear how various scales of turbulent motions embedded in the 'turbulent' contribution component (i.e. embedded in the Reynolds shear stress $-\langle uv\rangle$ that can be represented by the uv cospectra) play their roles in contributing to the 'turbulent' contribution component itself (as well as to the total).

Secondly, it remains unknown whether/how the contributions of different scales of turbulent motions in OCFs differ with those in other wall-bounded flows, especially with CCFs, given the similarities shared by the two flows. For instance, at smooth-walled conditions, the two flows shared the same FIK identity expression (1.1), and both the 'laminar' and 'turbulent' contribution components (i.e. $C_{f1,FIK}$ and $C_{f2,FIK}$) are expected to be identical when the bulk Reynolds numbers of the two flows are the same. However, the contributions from different scales of turbulent motions could still be different if turbulent motions embedded in the uv cospectra exhibit any differences, which could be expected since the outer boundaries of the two flows are different (i.e. a free surface presents in OCFs). To our knowledge, quantitative comparisons of the turbulent motions embedded in uv cospectra between the two flows are still lacking.

The key objectives of the present study are to clarify the above two issues, i.e. the contributions of various turbulent scales to $\langle\tau_w\rangle$ in OCFs, and the difference between OCFs and CCFs in this regard. To achieve this purpose, the FIK identity decomposition method combined with a scale decomposition is adopted to decompose $\langle\tau_w\rangle$ in smooth-walled open channel. The smooth wall condition is considered herein to facilitate comparisons of OCFs and CCFs and the main reasons for adopting the FIK identity method will be explained in § 2.3. The organization of the paper is as follows. Section 2 describes the flow datasets and decomposition method for $\langle\tau_w\rangle$. Section 3 presents the main results, including the 'laminar' and 'turbulent' contributions, and scale decomposed 'turbulent' contributions to $\langle\tau_w\rangle$ in OCFs; comparisons between OCF and CCF are also performed. Finally, § 4 gives a brief summary of major findings.

2. Datasets and methodology

The coordinates x, y and z correspond to the streamwise, wall-normal and spanwise directions, respectively; U, V, W refer to the corresponding mean velocities, and u, v, w to respective fluctuations. The superscript '+' indicates normalization with inner-scale units, e.g. $U^+ = U/u_\tau$ for velocity, and $y^+ = y/(\nu/u_\tau)$ for length. Angle brackets and a superscript prime denote the ensemble average and root mean square of a given quantity, respectively.

2.1. *Open channel flow datasets*

Six open channel flow cases were considered with the friction Reynolds number Re_τ ranging from 550 to 2400 (see table 1), including one direct numerical simulation (DNS) case at $Re_\tau = 550$ (Wang & Richter 2019) and five experimental cases at $Re_\tau = 600$, 1000, 1500, 1900, and 2400 (Duan *et al.* 2020*a*). Hereafter, the six cases are denoted as OCFDNS550, OCF600, OCF1000, OCF1500, OCF1900, and OCF2400, respectively.

The OCFDNS550 case corresponds to the simulation case 7 in Wang & Richter (2019) (see table 1 therein). The only difference that should be mentioned here is the friction

https://doi.org/10.1017/jfm.2021.236 Published online by Cambridge University Press

Open channel flow datasets						
Case	Data type and source	Re_τ	Re_b	$L_x \times L_y(\times L_z)$	TU_b/h	$\Delta x^+ \times \Delta y^+(\times \Delta z^+)$
OCFDNS550	DNS (Wang & Richter 2019)	539	9782	$12\pi h \times 1h \times 2\pi h$	360	$9.9 \times (1.0, 7.1) \times 6.6$
OCF600	Experiments with PIV (Duan *et al.* 2020*a*)	614	11 462	$0 < y \leq h$	18 751	5.1×5.1
OCF1000		1030	20 905		11 218	6.1×6.1
OCF1500		1508	31 889		13 427	9.6×9.6
OCF1900		1903	41 496		14 040	11.1×11.1
OCF2400		2407	54 140		15 793	13.9×13.9
Closed channel flow datasets for comparisons						
Case	Data type and source	Re_τ	Re_b	$L_x \times L_y(\times L_z)$	TU_b/h	$\Delta x^+ \times \Delta y^+(\times \Delta z^+)$
CCFDNS550	DNS (Lee & Moser 2015, 2019)	543	10 000	$8\pi h \times 2h \times 3\pi h$	250	$8.9 \times (0.02, 4.5) \times 5.0$
CCFDNS1000		1001	20 000			$10.9 \times (0.02, 6.2) \times 4.6$
CCFDNS2000		1995	43 478			$12.2 \times (0.02, 8.2) \times 6.1$
CCFDNS550VL	DNS (Lozano-Durán & Jiménez 2014)	547	10 060	$60\pi h \times 2h \times 6\pi h$	90	$12.6 \times (0.02, 6.7) \times 5.0$
CCF1000	Experiments with HWA (Deshpande, Monty & Marusic 2020)	988	19 718	28 y positions ($75 \leq y^+ \leq Re_\tau$)	14 000	$\Delta y^+_{min} = 9, \Delta y^+_{max} = 20$
CCF1600	Experiments with HWA (Balakumar 2005; Balakumar & Adrian 2007)	1584	33 700	8 y positions $0.12 \leq y/h \leq 0.87$	—	—

Table 1. A summary of the open channel flow and closed channel flow datasets. $Re_\tau = u_\tau h/\nu$ and $Re_b = U_b h/\nu$ are the friction and bulk Reynolds numbers, respectively. L_x, L_y and L_z are the simulated/measured domain sizes along x, y and z directions. T is the simulating (or sampling) duration. Δx^+, Δy^+, and Δz^+ are the inner-scaled velocity vector spacings along x, y and z directions. For the numerical case, the two values in Δy^+ denote the spacings at the wall and channel centre/surface respectively. The readers are referred to Appendix A for a detailed data accuracy verification for the above datasets.

velocity u_τ. The u_τ in Wang & Richter (2019) was precalculated according to the preset pressure gradient $\partial P/\partial x$ driving the flow through $\partial P/\partial x = -(\langle\tau_w\rangle/h) = -(\rho u_\tau^2/h)$, while u_τ in this study is post determined according to $\langle\tau_w\rangle$ obtained with the simulated flow fields. Though the difference between the two is relatively small (2 %), it matters given that the present research focus is the wall-shear stress, and the post determined one is adopted herein. The dimensions of the simulation domain $L_x \times L_y \times L_z$ (streamwise $\times$ wall-normal $\times$ spanwise) are $12\pi h \times h \times 2\pi h$, which are sufficiently large to resolve most portions of energetic turbulent motions.

The experimental data are from the measurements conducted by Duan *et al.* (2020*a*), with five cases $Re_\tau = 600$, 1000, 1500, 1900, and 2400, respectively. The aspect ratio B/h (B is the channel width) is greater than 7.2 in all cases, well exceeding the threshold value of 5 to ensure two-dimensional flows at the flume centre region (Nezu & Nakagawa 1993; Nezu 2005). Two-dimensional particle image velocimetry (PIV) measurements were conducted in the streamwise-vertical (x–y) plane at spanwise centre of the flume. The measurement plane was located greater than $210h$ away from the flume entrance to allow the flow to be sufficiently developed. Fully time-resolved PIV measurements were performed with appropriate sampling duration (T, TU_b greater than $10\,000h$) and sampling frequency (interval between successive velocity field $\Delta T^+ < 1$) to allow all scales of turbulent motions being of interest to be well resolved (Baars, Hutchins & Marusic 2016; Baidya *et al.* 2017). The velocity fields were obtained based on a multi-pass and multi-grid window deformation PIV algorithm (which is similar to that in Scarano 2002) with the initial and final interrogation window sizes chosen to be 64 pixels $\times$ 64 pixels and 16 pixels $\times$ 16 pixels, respectively, with a 50 % overlap. The resultant inner-scale normalized vector spacing is $5 \sim 14$.

2.2. *Closed channel flow datasets for comparisons*

For comparison purposes, six closed channel flow cases were also considered (as summarized in table 1), including three DNS cases at $Re_\tau = 550$, 1000, 2000 with normal streamwise domain sizes of $L_x = 8\pi h$ (Lee & Moser 2015, 2019), one DNS case at $Re_\tau = 550$ with a very long streamwise domain size of $L_x = 60\pi h$ (Lozano-Durán & Jiménez 2014), and two experimental cases at $Re_\tau = 1000$ (Deshpande *et al.* 2020) and 1600 (Balakumar 2005; Balakumar & Adrian 2007).

For the former three CCF DNS cases with $L_x = 8\pi h$ (denoted as CCFDNS550, CCFDNS1000, and CCFDNS2000), the raw statistics and spectra can be freely accessed from the website https://turbulence.oden.utexas.edu/. This open-access CCF DNS database is one of the most widely used databases in the literature (see e.g. Fan *et al.* (2019*a*), Zhang *et al.* (2019), Hu, Yang & Zheng (2020), etc.) and the simulation details and validations can be found in Lee & Moser (2015) and Lee & Moser (2019). And for the last CCF DNS at $Re_\tau = 550$ with $L_x = 60\pi h$ (denoted as CCFDNS550VL) (Lozano-Durán & Jiménez 2014), it is a complement to the CCFDNS550 case. To the authors' knowledge, such a long domain simulation is so unique in the literature that it not only allows resolving almost all scales of energetic turbulent motions but also allows verifying the accuracy of smaller domain size simulation results (namely whether the domain sizes of CCFDNS550 with $L_x = 8\pi h$ and OCFDNS550 with $L_x = 12\pi h$ are already large enough to yield accurate results). Both of the two aspects will be further discussed in § 3.

The two experimental cases at Re_τ=1000 (Deshpande *et al.* 2020) and 1600 (Balakumar 2005; Balakumar & Adrian 2007) (denoted as CCF1000 and CCF1600) are fully time-resolved velocity measurements performed with hot-wire anemometry (HWA), from

which the streamwise and wall-normal velocity components are simultaneously measured. Accordingly, the streamwise (co-)spectra of the streamwise and wall-normal velocity fluctuations were obtained. In CCF1000 case, measurements were conducted at 28 y positions covering almost the whole wall layer ($75 \leq y^+ \leq Re_\tau$). While in CCF1600 case, only 8 y position measurements within $0.12 \leq y/h \leq 0.87$ are available.

In summary, the numerical and experimental CCF cases complement each other for comparison with OCFs. The DNS cases were mainly for comparison of the 'laminar' and 'turbulent' contribution components of $\langle \tau_w \rangle$ between OCFs and CCFs, which will be presented in § 3.1. The CCFDNS550 and CCFDNS550VL cases were further used for comparisons of the scale-decomposed 'turbulent' contribution component with that of OCF DNS case at identical Re_τ, i.e. the OCFDNS550 case. For the remaining CCF DNS cases at higher Re_τ (CCFDNS1000 and CCFDNS2000), due to the absence of OCF DNS at identical Re_τ herein, such comparisons between OCF and CCF using DNS cannot be made. Note also that due to the inherent difference between experimental and DNS spectra (i.e. the experimental spectra are obtained from temporal velocity data and a time-space transformation is made through Taylor's hypothesis; while the DNS spectra is directly obtained from the spatial velocity data), the experimental OCF cases at comparable Re_τ are also not appropriate for direct comparisons with the CCFDNS1000 and CCFDNS2000 cases. The main limitation of the comparisons of scale-decomposed 'turbulent' contribution component between OCFDNS550, CCFDNS550, and CCFDNS550VL cases is the low Reynolds number. Based on such consideration, two experimental CCF cases (CCF1000 and CCF1600) were further considered to allow direct comparisons with the experimental OCF cases at identical and higher Re_τ.

2.3. *Decomposition method of the mean wall-shear stress*

The FIK identity method defined in (1.1) was finally adopted to decompose the mean wall-shear stress. Here instead of the RD identity (as well as the method of Yoon *et al.* 2016), the FIK identity was finally adopted mainly based on two considerations: the FIK identity is more often used in previous studies regarding OCFs (as can be seen in the introduction); the FIK identity (decomposing C_f into 'laminar' and 'turbulent' components) allows quantifying the contributions of turbulent motions to the mean wall-shear stress, which is exactly the focus of this study.

Since only the FIK identity method was considered, we would simply denote the two decomposed terms in the right-hand side of (1.1) as C_{f1} and C_{f2} for brevity. For simplicity of representation, as that did in Deck *et al.* (2014) for TBLs, here we would rewrite C_{f2} as

$$C_{f2} = \int_0^1 F_R \, \mathrm{d}\left(\frac{y}{h}\right), \tag{2.1}$$

where $F_R = -6(1 - y/h)(\langle uv \rangle / U_b^2)$ represents the weighted contribution of the Reynolds shear stress to $\langle \tau_w \rangle$. The ratios of C_{f1}/C_f and C_{f2}/C_f provide a simple and straightforward quantification of the 'laminar' and 'turbulent' contributions to $\langle \tau_w \rangle$, respectively.

To further break down the overall contribution of C_{f2}/C_f to various scales, it needs a scale decomposition of C_{f2}, which can be performed in terms of streamwise scales (streamwise wavenumber k_x or equivalently streamwise wavelength $\lambda_x = 2\pi/k_x$) or spanwise scales (spanwise wavenumber k_z or spanwise wavelength $\lambda_z = 2\pi/k_z$) or both of them. In the present study, we would confine our discussions on the decomposition along streamwise direction only.

At a considered y location, the Reynolds shear stress cospectra (termed as uv cospectra for short) can be defined as

$$\Phi_{uv}(k_x) = c\left\langle Re[\tilde{u}(k_x)\tilde{v}^*(k_x)]\right\rangle, \tag{2.2}$$

where the upper tilde indicates the Fourier transform of a given fluctuating velocity component (for example, $\tilde{u}(k_x) = \mathcal{F}[u]$ is the Fourier transform of u) in either x or time t, depending on the data. The superscript asterisk ($*$), Re[$\cdot$], and angle brackets ($\langle\rangle$) in (2.2) denote the complex conjugate, real part of a complex number, and ensemble averaging, respectively, while c is a constant determined by satisfying $\langle uv\rangle = \int_0^\infty \Phi_{uv}(k_x)\,\mathrm{d}k_x$. For the temporal data (i.e. the experimental flow cases), a frequency f to wavenumber k_x transformation is performed by invoking Taylor's hypothesis: $k_x = 2\pi f/U_c$, where U_c is the convection velocity at location y that is generally assumed to be the local mean streamwise velocity U if U_c is unavailable.

Based on uv cospectra Φ_{uv}, the spectra of F_R, denoted as Φ_{F_R}, can be given by

$$\Phi_{F_R} = -6\left(1 - \frac{y}{h}\right)\frac{\Phi_{uv}}{U_b^2}, \tag{2.3}$$

so that $F_R = \int_0^\infty \Phi_{F_R}\,\mathrm{d}k_x$. And finally C_{f2} is expressed as

$$C_{f2} = \int_0^1 \int_0^\infty \Phi_{F_R}\,\mathrm{d}\,(k_x)\,\mathrm{d}\left(\frac{y}{h}\right). \tag{2.4}$$

It can be seen that Φ_{F_R} in (2.4), which is a function of motion scales (wavenumber k_x or wavelength λ_x) and y position, actually provides a local contribution (from a given scale of turbulent motions at a given y position) to C_{f2}. And if (2.4) is divided by C_f and rewritten as

$$\frac{C_{f2}}{C_f} = \int_{-\infty}^0 \int_{-\infty}^\infty \frac{k_x(y/h)\,\Phi_{F_R}}{C_f}\mathrm{d}\,(\ln(k_x))\,\mathrm{d}\left(\ln\left(\frac{y}{h}\right)\right), \tag{2.5}$$

then plotting $k_x(y/h)\,\Phi_{F_R}/C_f$ in the (λ_x, y) plane with logarithmic scales for both y and λ_x yields a representation of the local contribution of a given scale at a given y position to C_f, namely to $\langle\tau_w\rangle$, as the local contribution is proportional to the volume located below the $k_x(y/h)\,\Phi_{F_R}/C_f$ surface.

Alternatively, (2.4) can be firstly integrated over all y positions to assess the contribution of a specific scale to C_{f2}. This motivates a definition of a kind of spectrum of C_{f2} (denoted as $\Phi_{C_{f2}}$), which depends on the scale of the contributing turbulent motions across the whole water depth (Deck *et al.* 2014). Then (2.4) could be rewritten as

$$C_{f2} = \int_0^\infty \underbrace{\int_0^1 \Phi_{F_R}\,\mathrm{d}\left(\frac{y}{h}\right)}_{\Phi_{C_{f2}}}\mathrm{d}\,(k_x) = \int_0^\infty \Phi_{C_{f2}}\,\mathrm{d}\,(k_x). \tag{2.6}$$

Similarly, dividing (2.6) with C_f and rewriting it as

$$\frac{C_{f2}}{C_f} = \int_{-\infty}^\infty \frac{k_x\Phi_{C_{f2}}}{C_f}\mathrm{d}\,(\ln(k_x)). \tag{2.7}$$

By plotting $k_x\Phi_{C_{f2}}/C_f$ as a function of wavelength λ_x in logarithmic scale, one can see the contribution of specific physical length scales to C_f, i.e. to $\langle\tau_w\rangle$, and the total area below the $k_x\Phi_{C_{f2}}/C_f$ curve equals the total 'turbulent' contribution to $\langle\tau_w\rangle$.

Case	Re_τ	Re_b	$C_{f,direct}$	C_{f1}	C_{f2}	C_f	C_{f1}/C_f (%)	C_{f2}/C_f (%)
OCFDNS550	539	9782	0.0061	0.0006	0.0054	0.0060	10.0	90.0
OCF600	614	11 462	0.0057	0.0005	0.0053	0.0058	9.0	91.0
OCF1000	1030	20 905	0.0049	0.0003	0.0046	0.0049	5.9	94.1
OCF1500	1508	31 889	0.0045	0.0002	0.0043	0.0045	4.2	95.8
OCF1900	1903	41 496	0.0042	0.0001	0.0041	0.0042	3.4	96.6
OCF2400	2407	54 140	0.0040	0.0001	0.0038	0.0039	2.8	97.2
CCFDNS550	543	10 000	0.0059	0.0006	0.0053	0.0059	10.2	89.8
CCFDNS1000	1001	20 000	0.0050	0.0003	0.0047	0.0050	6.0	94.0
CCFDNS2000	1995	43 478	0.0042	0.0001	0.0041	0.0042	3.3	96.7

Table 2. The friction coefficient and its 'laminar' and 'turbulent' constituents.

3. Results

3.1. *The 'laminar' and 'turbulent' contributions*

The total friction coefficient C_f and its two components, C_{f1} and C_{f2}, are firstly quantified and summarized in table 2, where both the results of present OCFs and those of CCFs are presented. Note that for the experimental cases, to avoid the magnitude effect of measured Reynolds shear stress on the estimation of C_{f2}, the raw measured Reynolds shear stress was modified based on the theoretical equation for the total stress, i.e. $-\langle uv\rangle + \nu(\partial U/\partial y) = u_\tau^2(1 - y/h)$. The estimated friction coefficient based on the FIK identity was compared with the directly calculated ones based on the definition ($C_{f,direct} = 2u_\tau^2/U_b^2$). Good agreement can be seen, as the relative error is confined within ± 1 % for all flow cases studied herein.

As expected to be seen in table 2, the total friction coefficient C_f, and its 'laminar' and 'turbulent' constituents (C_{f1} and C_{f2}) are approximately identical between OCFs and CCFs at identical Reynolds numbers, demonstrating the commonality of 'laminar' and 'turbulent' contributions to $\langle\tau_w\rangle$ within the two flows. It can be also seen from table 2 that the 'turbulent' portion contributes over 90 % of $\langle\tau_w\rangle$ in the present Reynolds number range, and its contributions increase as the Reynolds number increases.

Further, since the 'turbulent' contributions result from a wall-normal integration of the weighted Reynolds shear stress across the whole wall layer, it is of interest to see the share of different y regions. This can be demonstrated by plotting the pre-multiplied integrand of C_{f2}/C_f, i.e. $y/h\ F_R/C_f$ (as can be readily seen in (2.1)), as a function of y/h in logarithmic scale and the area below the $y/h\ F_R/C_f$ curve is proportional to the contribution to C_f, i.e. to $\langle\tau_w\rangle$. One such plot of $y/h\ F_R/C_f$ is presented in figure 1(*a*). For comparison, the results of the aforementioned comparable CCF cases (CCFDNS550 to CCFDNS2000) are also included. As seen in figure 1(*a*), the outer region represents the most significant part of the contributions to $\langle\tau_w\rangle$, with the maximum universally residing within $y/h = 0.3 \sim 0.4$. As expected, when the Reynolds number increases, the local contribution at all y positions increases, and the total contribution increases accordingly. Approximately identical profiles are observed between OCF and CCF cases at identical Reynolds numbers; this further demonstrates the similarity between the two flows.

Figure 1(*b*) shows the corresponding cumulative turbulent contribution to $\langle\tau_w\rangle$ (denoted as $Cum_{turb}(y)$ for brevity) obtained by integrating the area below $y/h\ F_R/C_f$ curve shown in figure 1(*a*). Noting that since only the turbulent contribution portion is considered, the curve value will not attain the value 100 % but the value C_{f2}/C_f for $y/h = 1$. It can be seen

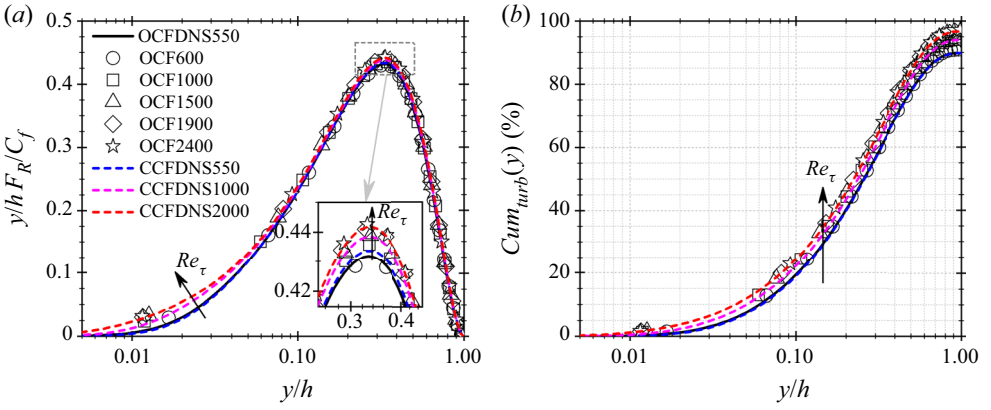

Figure 1. Wall-normal distributions of (*a*) $y/h\ F_R/C_f$ and (*b*) cumulative turbulent contribution to $\langle\tau_w\rangle$, $Cum_{turb}(y)$. Noting that Cum_{turb} only takes the turbulent contribution portion into account, thus it will not attain the value 100 % for $y/h = 1$.

that the region below $y/h = 0.2$ contributes to about $40 \sim 47$ % of $\langle\tau_w\rangle$, while the region of $y/h > 0.2$ makes a contribution of about 50 %.

3.2. *Scale decomposition of the 'turbulent' contribution*

The results shown in § 3.1 have demonstrated that OCFs and CCFs are almost identical in the 'turbulent' contribution to $\langle\tau_w\rangle$. The breakdown of the contribution, however, differs in the two flows. This is further demonstrated by performing a scale decomposition of the 'turbulent' contribution portion.

As it has been described in § 2.3, plotting $k_x(y/h)\ \Phi_{F_R}/C_f$ in the (λ_x, y) plane with logarithmic scales for both y and λ_x could give a representation of the local contribution of a given scale at a given y position to $\langle\tau_w\rangle$ (this can be readily seen in (2.5) in § 2.3). One such plot is presented in figure 2 for all the six OCF cases studied herein. For each case, both inner-scale (see the top (λ_x^+) and right (y^+) axes) and outer-scale (see the bottom (λ_x/h) and left (y/h) axes) units are presented for better demonstration of the scaling characteristics.

The features revealed in outer units will be first discussed. Similar to that shown in figure 1, figure 2 also shows the most significant local contributions in the outer region within $y/h = 0.3 \sim 0.4$. In terms of the scales, the turbulent motions with streamwise wavelength $\lambda_x = 1 \sim 2h$ make the highest contribution at all Reynolds number flow cases. As the Reynolds number increases, another dominant contribution mode at $\lambda_x = O(10h)$ becomes increasingly apparent. By checking the wavelength of the two peaks, it can be readily known that they correspond to the well-documented large-scale motions (LSMs) and very-large-scale motions (VLSMs) (Kim & Adrian 1999; Guala, Hommema & Adrian 2006; Balakumar & Adrian 2007; Monty *et al.* 2009; Cameron, Nikora & Stewart 2017; Duan *et al.* 2020*a*; Peruzzi *et al.* 2020, to name a few), respectively. The presence of double peaks in $k_x(y/h)\ \Phi_{F_R}/C_f$ is easy to understand since $k_x(y/h)\ \Phi_{F_R}/C_f$ (with $\Phi_{F_R} = -6(1 - y/h)(\Phi_{uv}/U_b^2)$) is actually a weighted and premultiplied uv cospectra where dominant modes of LSMs and VLSMs are present.

When observed in inner-scale units, both y^+ and λ_x^+ of the two peaks increase with the Reynolds number. Based on these observations, it is known that the local contributions of turbulent motions to $\langle\tau_w\rangle$ scale in outer units rather than inner units. Even though

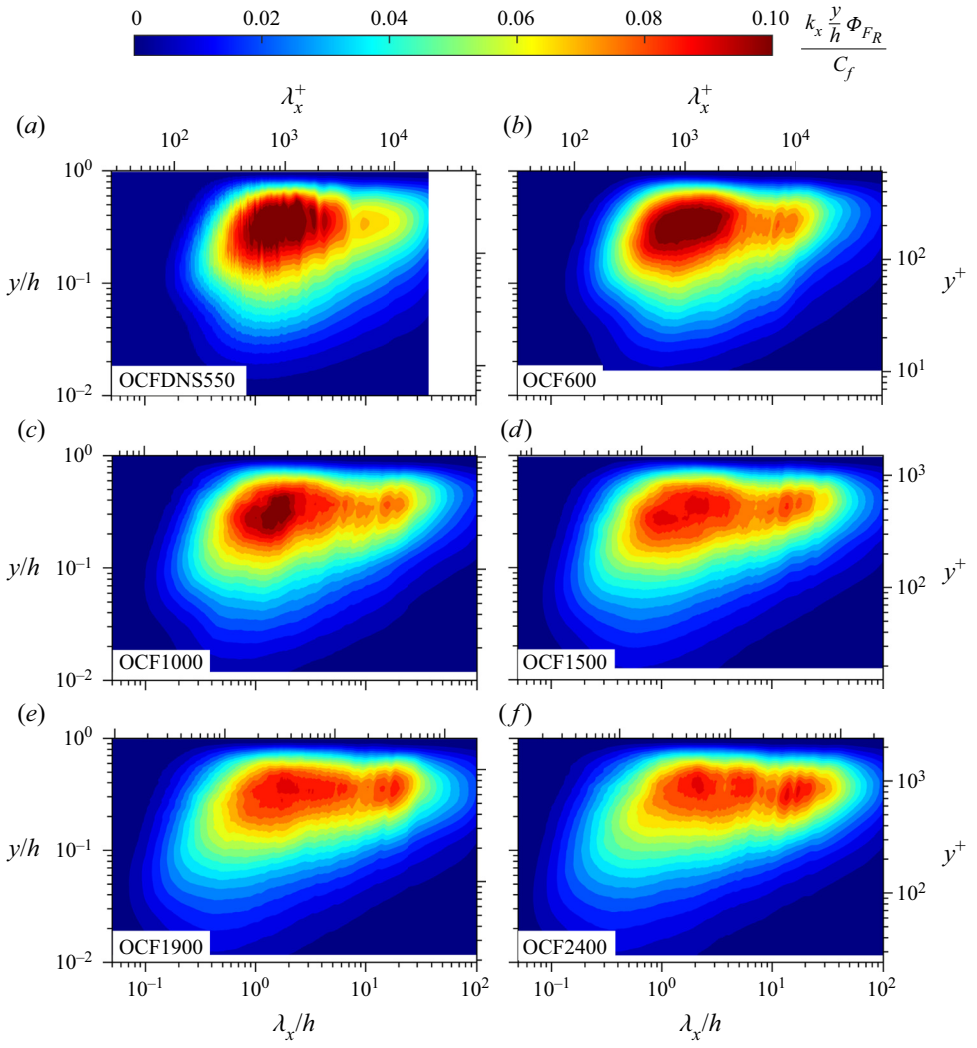

Figure 2. Local turbulent contribution $k_x(y/h)\,\Phi_{F_R}/C_f$ to $\langle\tau_w\rangle$. Panels (*a–f*) are the six open channel flow (OCF) cases studied herein respectively with the flow cases labelled in the lower left corner.

other scaling characteristics may be observed when other $\langle\tau_w\rangle$ decomposition methods are adopted (for instance the RD identity method (Renard & Deck 2016) and Yoon *et al.* (2016)'s method), the physical meanings of the results revealed by these methods are different from the present one (namely scale-dependent turbulent contributions to $\langle\tau_w\rangle$). Detailed discussions on the scaling characteristics in different $\langle\tau_w\rangle$ decomposition methods are out of the focus herein, given which they will be not discussed any further.

Integrating the local contribution (scale and position-dependent) over the whole water depth leads to the contribution of physical length scales to $\langle\tau_w\rangle$. Returning to (2.7) in § 2.3, this can be expressed by plotting $k_x\Phi_{C_{f2}}/C_f$ as a function of wavelength λ_x in logarithmic scale. One such plot for all present OCF cases is shown in figure 3, where inner- and outer-scale normalized length scales are used in figures 3(*a*) and 3(*b*), respectively. It is

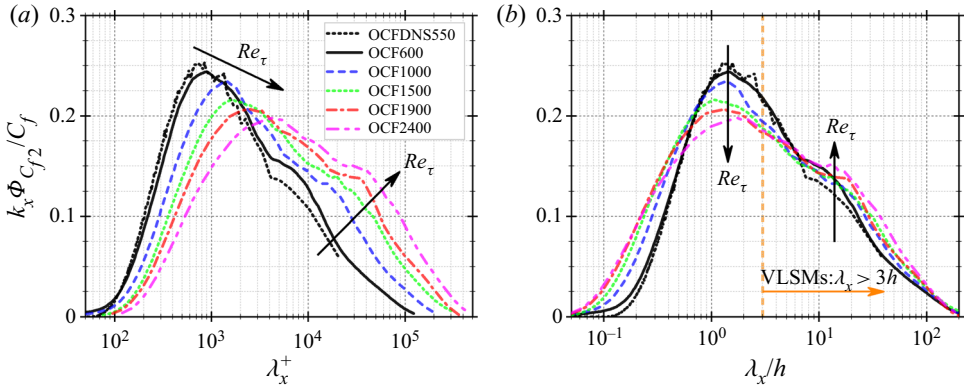

Figure 3. Contribution $k_x\Phi_{C_{f2}}/C_f$ of physical length scales to $\langle\tau_w\rangle$, where inner- and outer-scale normalized length scales are used in (*a*,*b*), respectively.

quite clear that the bimodal phenomenon observed in figure 2 becomes more visible in figure 3.

As can be seen in figure 3(*a*), the curves presented in λ_x^+ gradually shift towards larger wavelength range as the Reynolds number increases, during which the magnitudes of $k_x\Phi_{C_{f2}}/C_f$ for the short-wavelength and long-wavelength peaks successively decrease and increase respectively (the trends are roughly marked by dark arrows). These trends observed in figure 3(*a*) indicate the gradually enhanced significance of larger scale contributions to $\langle\tau_w\rangle$ at higher Reynolds numbers.

When the curves are presented in λ_x/h (see figure 3*b*), no obvious global offset along wavelength direction can be observed, which in turn further demonstrates the contributions of turbulent motions to $\langle\tau_w\rangle$ scale in outer units. Consistent with the results shown in figure 2, the short- and long-wavelength peaks are roughly located at $\lambda_x = 1 \sim 2h$ and $O(10h)$, corresponding to the dominant contributions from LSMs and VLSMs, respectively. Following the widely used separation wavelength value in the literature (Guala *et al.* 2006; Balakumar & Adrian 2007; Zhong *et al.* 2015; Duan *et al.* 2020*a*), $\lambda_x = 3h$ was adopted here to separate LSMs and VLSMs, as has been marked by vertical orange dashed lines in figure 3(*b*). Comparisons of the five experimental flow cases with Re_τ ranging from 600 to 2400 (see OCF600 to OCF2400) show that as the Reynolds number increases, the contribution from LSMs (at $\lambda_x = 1 \sim 2h$) gradually decreases, while the contribution from VLSMs tends to increase.

As can be also seen in figure 3, good agreements observed between the OCFDNS550 and OCF600 cases indicate that the application of Taylor's hypothesis in the experimental cases for making a time-space transformation exert negligible effects, at least at this low Reynolds number case. This may not hold for high Re_τ cases where the scale separation between inner and outer scale turbulent motions becomes larger, and the variations of the convection velocity U_c over different scales and its deviations from the local mean streamwise velocity U both impose challenges on the validity of using U as the surrogate of U_c in Taylor's hypothesis. Accordingly, the real curve of $k_x\Phi_{C_{f2}}/C_f$ could differ from that shown in figure 3 for higher Re_τ. However, in terms of the Re_τ considered here (at low-to-moderate level with the highest $Re_\tau = 2400$), such kind of difference is expected to be small based on the aforementioned good agreements between the experimental and DNS cases at $Re_\tau = 550$. More importantly, though the real $k_x\Phi_{C_{f2}}/C_f$ curve could differ with that shown in figure 3 in magnitude (perhaps also a slightly offset along

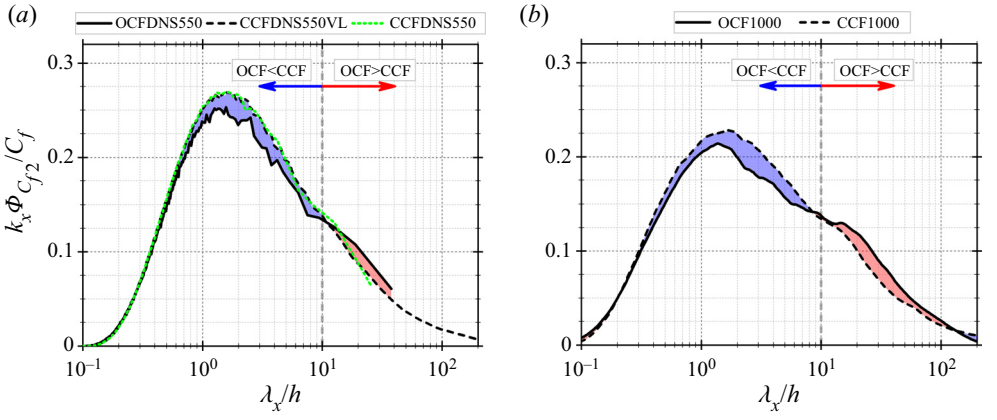

Figure 4. Comparison of the contribution $k_x\Phi_{C_{f2}}/C_f$ of physical length scales to $\langle\tau_w\rangle$ between OCF and CCF cases at $Re_\tau = 550$ (a) and 1000 (b), where the solid and dashed lines represent OCF and CCF cases, respectively. Red and blue shaded regions indicate the higher and lower value regions in OCF, respectively. Noting that both CCFDNS550 and CCFDNS550VL cases are shown in (a) for demonstrating the potential streamwise domain size effect, and the blue and red shaded regions correspond to the comparison between OCFDNS550 and CCFDNS550VL cases.

the wavelength direction), it would not affect the general findings herein (i.e. the two dominant contributing modes at LSMs ($\lambda_x = 1 \sim 2h$) and VLSMs ($\lambda_x = O(10h)$), and Reynolds number dependent trend that the contribution from VLSMs increases as Reynold number increases), given that both of them are well consistent with the consensus in the wall-turbulence community.

3.3. *Comparison of the scale decomposed contribution between OCF and CCF*

Comparisons of the scale-decomposed contribution between OCF and CCF are further made by plotting the results together. Figure 4(a) first presents the $k_x\Phi_{C_{f2}}/C_f$ curves for the numerical cases at $Re_\tau = 550$ (i.e. OCFDNS550 and CCFDNS550(VL)), where the solid and dashed lines denote the OCF and CCF cases, respectively. Noting that although one of the two CCF DNS cases (CCFDNS550 (with streamwise domain size $L_x = 8\pi h \approx 25h$) and CCFDNS550VL (with $L_x = 60\pi h \approx 190h$)) is already enough for comparison purpose, both of them are presented herein mainly for demonstrating the potential streamwise domain size effect. For better demonstration of the differences, the regions between the curves are coloured, with red and blue indicating higher and lower value regions in OCF, respectively. Between the two CCF cases, the CCFDNS550VL case was used to colouring the difference given the larger wavelength range it resolves.

Though the curve shapes are generally similar, differences between the OCF and CCF curves can still be observed in figure 4(a). In the wavelength range of $\lambda_x > O(10h)$ (roughly corresponding to the typical wavelength of VLSMs), the $k_x\Phi_{C_{f2}}/C_f$ value in OCF is higher than that in CCF, indicating higher contributions of turbulent motions to $\langle\tau_w\rangle$ in the corresponding wavelength range in OCF. While in the wavelength range of $\lambda_x < O(10h)$, the $k_x\Phi_{C_{f2}}/C_f$ value in OCF is lower than that in CCF. Almost identical curves observed for CCFDNS550 and CCFDNS550VL cases give a verification that the domain size of $8\pi h \approx 25h$ is long enough to yield accurate results, based on which the results of OCFDNS550 case based on a domain size of $12\pi h \approx 38h$ are also expected to be accurate enough. Accordingly, these observed differences of $k_x\Phi_{C_{f2}}/C_f$ between OCF

and CCF can be regarded as physical facts, rather than the limited streamwise domain size induced artefacts.

Figure 4(*b*) further presents the comparison of $k_x\Phi_{C_f2}/C_f$ between OCF and CCF at $Re_\tau = 1000$ (experimental OCF1000 and CCF1000 cases). Noting that $k_x\Phi_{C_f2}/C_f$ shown in figure 4(*b*) is estimated from the data within $75 \leq y^+ \leq Re_\tau$, for both OCF1000 and CCF1000 cases, because the CCF1000 case data are limited within this y range. Such an estimation of $k_x\Phi_{C_f2}/C_f$ is sufficient accurate (the total area below the curve equals to $0.95(C_{f2}/C_f)$, meaning that 95 % of the real value (C_{f2}/C_f) has been captured) to allow a reliable comparison of $k_x\Phi_{C_f2}/C_f$ between OCF and CCF. Similar differences observed in both figures 4(*a*) and 4(*b*) give further supports that the observed differences of $k_x\Phi_{C_f2}/C_f$ between OCF and CCF, namely higher and lower values in $\lambda_x > O(10h)$ and $\lambda_x < O(10h)$ range of OCF, are indeed physical.

These observed differences of $k_x\Phi_{C_f2}/C_f$ between OCF and CCF can be preliminarily clarified by checking the difference in the spectrum (u, v, and uv).

The premultiplied u and v spectra, and uv cospectra at multiple y positions are compared between OCF and CCF at comparable Reynolds numbers in figure 5. The DNS cases at $Re_\tau = 550$ (OCFDNS550 and CCFDNS550VL) are first presented in figure 5(*a*), where the u spectra, v spectra and uv cospectra are shown in columns (ii) to (iv), respectively, with the solid and dashed lines indicating OCF and CCF, respectively. As seen in figure 4, the regions between the curves are coloured for a better demonstration of the differences. To facilitate explanation, the profiles of turbulence intensities and Reynolds shear stress are presented in the leftmost column (i), where the solid and dashed lines again indicate OCF and CCF, respectively, and different statistical quantities are distinguished by colour.

Comparisons of the turbulent quantities (column (i) of figure 5*a*) again reveal the long documented unique feature of turbulent kinetic energy (TKE) redistribution in the near free surface region of OCF (Komori *et al.* 1993; Nezu & Nakagawa 1993; Zhong *et al.* 2015), i.e. the wall-normal turbulence intensity is weakened while the streamwise one is enhanced. Since the turbulence intensities result from a superposition of various scales of turbulent motions, the differences in turbulence intensities indicate the presence of differences in turbulent motions. To reveal these expected differences, the (co)spectra at typical y positions ($y/h = 0.2$, 0.5, 0.8, 0.95, as marked in column (i) of figure 5*a*) are shown in columns (ii) to (iv) of figure 5(*a*), where the spectral curves at different y locations are shown from bottom to top with appropriate upward offsets on each higher y position line. To make the differences of uv cospectra between OCF and CCF more readable, the uv cospectra at the last two higher y positions are multiplied by a constant (as marked in column (iv)).

Let's first focus on the u spectra (column (ii) of figure 5*a*). As expected, in the near-wall positions (e.g. $y/h = 0.2$), the curves of OCF and CCF are roughly the same. While moving away from the wall, the area under the OCF curve becomes greater than that of CCF because of higher streamwise turbulence intensity in OCF. By checking the wavelength, it can be seen that the extra area is mainly contributed from VLSMs. These observed differences of the premultiplied u spectra between OCF and CCF are well consistent with the authors' recent findings (Duan *et al.* 2020*a*), and both demonstrate that VLSMs in OCF are stronger than those in CCF. Then we could know that in the wavelength range of $\lambda_x > O(10h)$ (roughly corresponding to the typical wavelength of VLSMs), the turbulent motions in OCF are stronger than those in CCF.

The v spectra (column (iii) of 5*a*), unlike the u spectra where the large scale turbulent motions (LSMs and VLSMs) play important roles, indicate that the dominant motions are mainly small scale motions (with the peak energy located at $\lambda_x < h$). Near the wall, the

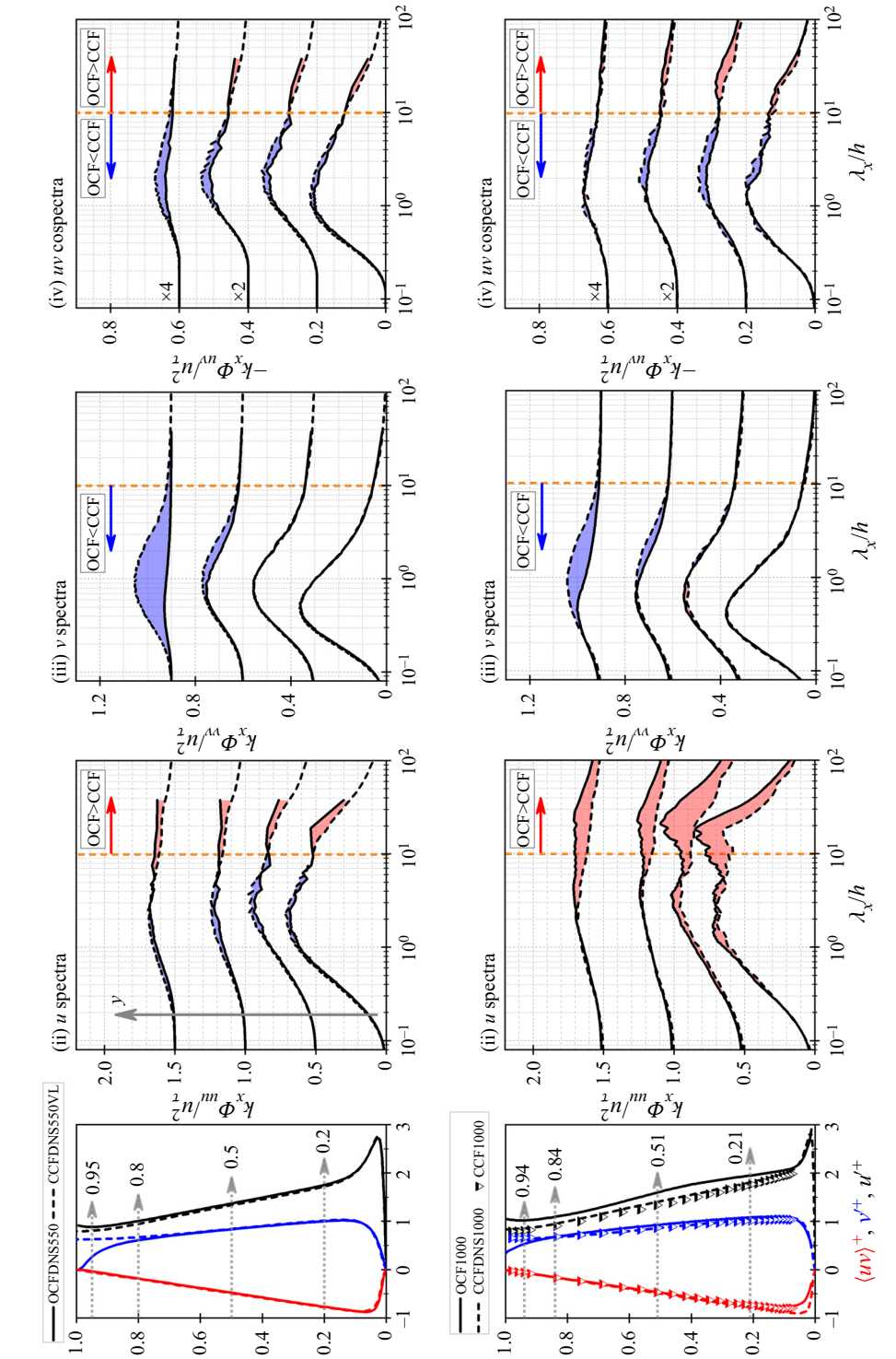

Figure 5. For caption see next page.

https://doi.org/10.1017/jfm.2021.236 Published online by Cambridge University Press

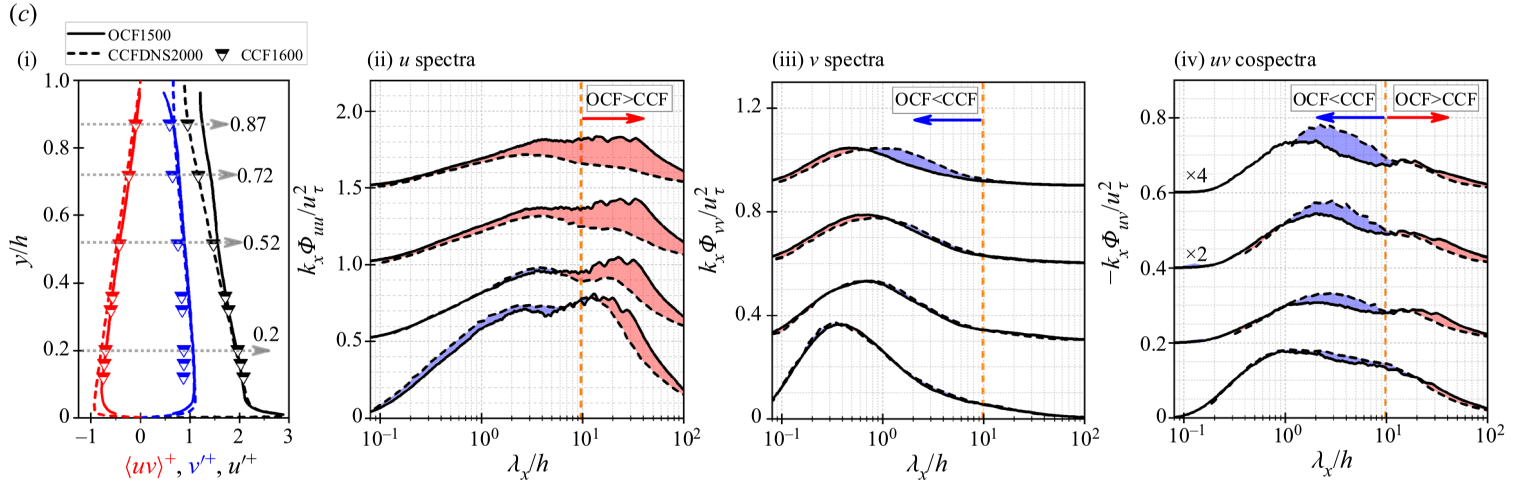

Figure 5 (cntd). Comparison of the statistical quantities and spectra between OCF and CCF at comparable Reynolds numbers, where column (i) presents the profiles of statistical quantities, and columns (ii) to (iv) show the u spectra, v spectra and uv cospectra at typical y positions respectively, with the positions marked by horizontal grey dashed arrows in column (i). Comparisons are made at $Re_\tau = 550$, 1000, and 1500 in (a), (b), and (c) respectively: (a) OCFDNS550 and CCFDNS550VL; (b) OCF1000 and CCF1000; (c) OCF1500 and CCF1600. In (b,c), since the statistical quantities for CCF1000 and CCF1600 cases are only available at discrete positions, the profiles of CCF DNS cases (CCFDNS1000 and CCFDNS2000) are presented additionally for verifying the accuracy of the experimental CCF cases; while in column (ii) to (iv) where the spectra are presented, the CCF spectra indeed refer to the experimental CCF1000 and CCF1600 cases rather than the DNS cases.

curves for OCF and CCF coincide well. While when approaching the free surface, the OCF curve becomes lower than that of CCF (see e.g. the curves at $y/h = 0.8$ and 0.95); this is reasonable because the wall-normal turbulence intensity in OCF is lower therein. Besides this magnitude difference, another noticeable difference lies in the shift of the peak (which indicates the most dominant motions) towards smaller scales in OCF when approaching the free surface.

The difference of uv cospectra between OCF and CCF is shown in column (iv) of figure 5(a). It is clear that OCF exceeds CCF in $\lambda_x > O(10h)$ range; in the $\lambda_x < O(10h)$ range, however, CCF turns to exceed OCF. From the comparisons of u and v spectra, it can be known that higher and lower uv cospectra in the two λ_x ranges of OCF are mainly contributed by the higher contribution of VLSMs revealed in u spectra, and lower contribution of smaller scales revealed in v spectra.

One main concern in the comparison of OCFDNS550 and CCFDNS550VL (figure 5a) is the low Reynolds number. To address such concern, similar comparisons were further performed for higher Reynolds number experimental cases, i.e. OCF1000 and CCF1000 (see figure 5b), and OCF1500 and CCF1600 (see figure 5c). In column (i) of figures 5(b) and 5(c) where statistical quantities are presented, we also included the CCF DNS cases (CCFDNS1000 and CCFDNS2000) for comparison and checking the reliability of CCF experimental data, which are only available at several discrete y positions. While in column (ii) to (iv) where spectra are presented, the CCF spectra indeed refer to experimental cases rather than DNS cases. The raw measured uv cospectra need to be rescaled to avoid the magnitude effect of the measured Reynolds shear stress on the comparison. This can be explained as follows: at a given position the Reynolds shear stress in theory $(-\langle uv\rangle)_{theory}$ should satisfy the theoretical equation $(-\langle uv\rangle)_{theory} + \nu(\partial U/\partial y) = u_\tau^2(1 - y/h)$. However, the measured one $(-\langle uv\rangle)_{measured}$ is generally not exactly equal to $(-\langle uv\rangle)_{theory}$. Given that the raw measured uv cospectrum $(\Phi_{uv})_{measured}$ is obtained by $(\langle uv\rangle)_{measured} = \int_0^\infty (\Phi_{uv})_{measured}\,\mathrm{d}k_x$, the magnitude of $(-\langle uv\rangle)_{measured}$ would directly affect the magnitude of $(\Phi_{uv})_{measured}$, and thus prevent reliable comparison of uv cospectra if $(-\langle uv\rangle)_{measured}$ is not rescaled to equal the theoretical one $(-\langle uv\rangle)_{theory}$. Therefore, for both OCF and CCF, uv cospectra are rescaled as $(\Phi_{uv})_{measured}\ (-\langle uv\rangle)_{theory}/(-\langle uv\rangle)_{measured}$. It can be seen that similar differences between OCF and CCF observed in figure 5(a) also occur in figures 5(b) and 5(c), demonstrating that increase in Reynolds number exerts no observable influence on such differences.

Beyond the above phenomenal explanations using spectra, we would give some more physical explains. As known to us, in the region close to the outer boundary of OCF and CCF, the velocity gradient is very small and $\nu(\partial U/\partial y)$ is negligible. Then $-\langle uv\rangle$ approximately follows a linear variation $-\langle uv\rangle = u_\tau^2(1 - y/h)$, and taking a derivative along y direction yields

$$\frac{\partial\,\langle uv\rangle}{\partial y} = \left\langle u\frac{\partial v}{\partial y}\right\rangle + \left\langle v\frac{\partial u}{\partial y}\right\rangle = \frac{u_\tau^2}{h}, \tag{3.1}$$

which holds both for OCF and CCF. The only difference between OCF and CCF is the upper boundary, i.e. a free surface presents in OCF, which affects the underlying turbulence by both dynamic and kinematic boundary conditions. The former one requires zero tangential stresses at the free surface and causes the surface layer which is a thin region adjacent to the free surface characterized by fast variations of the horizontal vorticity, while the latter one requires no mass flux at the free surface and produces the blockage layer within which TKE redistribution phenomena are observed. According to a

recent DNS study from Bauer (2015), the blockage layer thickness was demonstrated to scale in outer units ($\sim 0.3h$).

Ideally, if the free surface in OCF is flat without fluctuations, the wall-normal velocity at the free surface is exactly zero and (3.1) can be written as

$$\left.\frac{\partial \langle uv\rangle}{\partial y}\right|_{y=h} = \left\langle u\frac{\partial v}{\partial y}\right\rangle. \tag{3.2}$$

By further invoking the continuity equation, (3.2) can be rewritten as

$$\left.\frac{\partial \langle uv\rangle}{\partial y}\right|_{y=h} = \left\langle u\frac{\partial v}{\partial y}\right\rangle = -\left\langle u\left(\frac{\partial u}{\partial x}+\frac{\partial w}{\partial z}\right)\right\rangle = -\left\langle \frac{1}{2}\frac{\partial u^2}{\partial x}\right\rangle - \left\langle u\frac{\partial w}{\partial z}\right\rangle. \tag{3.3}$$

At steady and uniform conditions, the flow is homogenous along x direction and the mean value of the derivative of any flow quantities in terms of x would be zero. Then we could have

$$\left.\frac{\partial \langle uv\rangle}{\partial y}\right|_{y=h} = \left\langle u\frac{\partial v}{\partial y}\right\rangle = -\left\langle u\frac{\partial w}{\partial z}\right\rangle = \frac{u_\tau^2}{h} > 0, \tag{3.4}$$

based on which it can be known that in the near free surface region the fluctuating velocity components statistically satisfy the following relations:

$$\left.\begin{array}{llll} \dfrac{\partial v}{\partial y} > 0 & \text{and} & \dfrac{\partial w}{\partial z} < 0, & \text{when } u > 0 \\ \dfrac{\partial v}{\partial y} < 0 & \text{and} & \dfrac{\partial w}{\partial z} > 0, & \text{when } u < 0 \end{array}\right\}. \tag{3.5}$$

The streamwise rotating motions satisfy (3.5) and can be explained by figure 6(a), where a pair of streamwise rotating motions is presented for demonstration. On the upwelling rotation sides, low momentum fluids are pumped up to the free surface, leading to $u < 0$ (see regions marked in blue). Accordingly, v and w gradually decrease and increase, respectively, when approaching the free surface, meaning that $\partial v/\partial y < 0$ and $\partial w/\partial z > 0$ on upwelling sides. While on the downwelling sides, the high momentum fluids at the free surface are pumped downwards to the wall, leading to $u > 0$ (see regions marked in red), $\partial v/\partial y > 0$ and $\partial w/\partial z < 0$. Analogically, for streamwise rotating motions with opposite rotation directions, the same relationships can be derived. As can be seen, all the flow features of streamwise rotating motions satisfy the derived relations in (3.5).

These streamwise rotation motions can develop into different sizes of streamwise vortices: when the vertical motions are weak and localized in the vicinity of the free-surface, the generated streamwise vortices are small in size and supposed to locally reside in the near free-surface region; while when the vertical motions are strong enough to penetrate the whole water depth (e.g. whole water depth ejections/sweeps), water-depth scaled streamwise vortices can be generated (see figure 6c) and have been well documented in the literature with different terminologies, e.g. super-streamwise vortices, roll cells, etc. (Adrian & Marusic 2012; Zhong *et al.* 2015, 2016). Although these streamwise vortices also persist near the outer boundary of CCFs, they are speculated to be less populated and weaker due to the absence of upper boundary restrictions on vertical motions, which can be readily seen from the much higher wall-normal turbulence intensity near the upper boundary of CCFs than that of OCFs (see column (i) of figure 5).

Above analysis focuses on the upper boundary (free surface) related motions. Now we would discuss the lower boundary (solid wall) related motions, specifically the

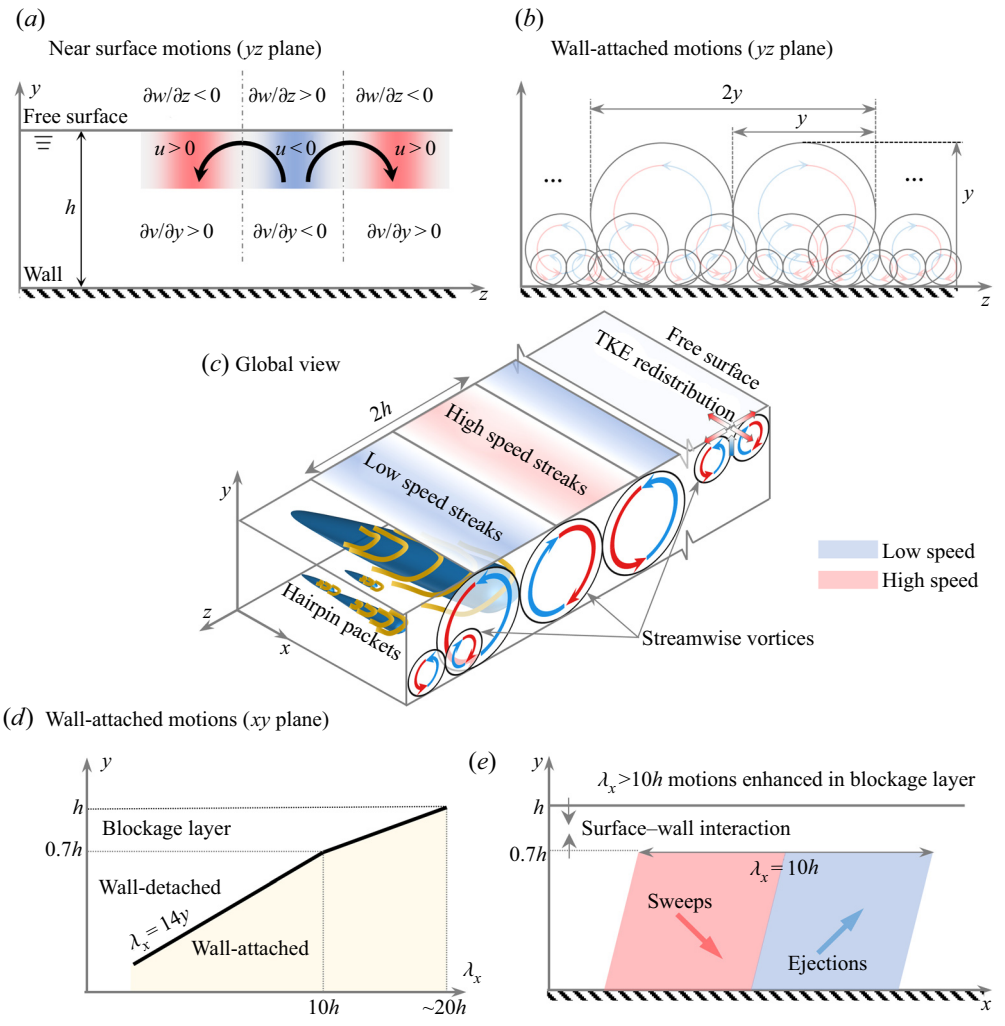

Figure 6. Schematic demonstration of the turbulent motions in OCFs to explain the possible mechanisms for the observed differences of scale-dependent turbulent contributions to $\langle \tau_w \rangle$ between OCF and CCF (i.e. higher and lower turbulent contribution in $\lambda_x > O(10h)$ and $< O(10h)$ range in OCF shown in figure 4.).

wall-attached ones that are relevant to wall-shear stresses studied herein. The earliest work can date back to Townsend's attached eddy hypothesis (Townsend 1976), where double-cone vortices were adopted as representative wall-attached motions, whose signatures in yz plane are counter-rotating streamwise vortices (as depicted in figure 6*b*). With better understandings of turbulent motions, it has been known that the representative wall-attached motions can be refined by hairpin packets (Marusic & Monty 2019), i.e. the transportation roles of hairpin packets give rise to these counter-rotating streamwise vortices. The wall-attached motions are geometrically self-similar in the log region with their scales proportional to the distance to the wall y. In yz plane, their diameters are roughly equal to y (figure 6*b*). In xy plane, Baars, Hutchins & Marusic (2017) and Duan *et al.* (2020*b*) demonstrated that the streamwise wavelength of wall-attached motions in TBL and OCF follows a linear variation with y as $\lambda_x = 14y$ up to $y/h = 0.7$ (where $\lambda_x = 10h$). Beyond $y/h = 0.7$, the streamwise wavelength increases more dramatically

and reaches $\lambda_x \sim 20h$ at the free-surface in OCF (Duan *et al.* 2020*b*) (as schematically shown in figure 6*d*). Since λ_x indicates a whole cycle of positive and negative velocity fluctuations, wall-attached motions represented by λ_x could be depicted as a whole cycle of sweeps and ejections in xy plane whose streamwise extend equals λ_x (see figure 6*e*).

Finally, based on the above discussions on the free-surface and wall related motions in OCFs, we could have a sound physical explanation on the observed differences of scale-dependent turbulent contributions to $\langle\tau_w\rangle$ between OCF and CCF (i.e. higher and lower turbulent contribution in $\lambda_x > O(10h)$ and $< O(10h)$ range in OCF, as shown in figure 4): the streamwise wavelength of wall-attached motions in the near free surface blockage layer ($y/h > 0.7$) reaches a value of $\lambda_x > 10h$. Such scale of wall-attached motions will interact with the free surface. The essential roles of the free surface in generating/promoting near-surface or whole water depth streamwise vortices would enhance the strength of these wall-attached motions whose spatial signatures are also streamwise vortices. Then these enhanced wall-attached motions with $\lambda_x > 10h$ would exert a stronger effect on the wall, thus leading to higher turbulent contributions to $\langle\tau_w\rangle$ in the $\lambda_x > O(10h)$ range of OCF, when compared to CCF. Given the total turbulent contributions are identical between OCF and CCF, higher contributions in the $\lambda_x > O(10h)$ range necessitate lower contributions in the $\lambda_x < O(10h)$ range.

3.4. *Contributions from different scale ranges*

For practical purpose, besides the scale-by-scale contributions, it is also desirable to know the contributions in a sense of scale range, i.e. the fractions of $\langle\tau_w\rangle$ contributed from a specific scale range of turbulent motions.

Figure 7 first shows the cumulative turbulent contribution profile $Cum_{turb}(\lambda_x)$ (corresponding to an integration of the area below the $k_x\Phi_{C_{f2}}/C_f$ curve), where $Cum_{turb}(\lambda_x)$ value at a specific wavelength indicates the total turbulent contributions from all scales of turbulent motions smaller than this given wavelength. Compared to $Cum_{turb}(y)$ shown in figure 1 which is an indication of the cumulative turbulent contribution to $\langle\tau_w\rangle$ vs y, $Cum_{turb}(\lambda_x)$ shown in figure 7 indicates the cumulative turbulent contribution to $\langle\tau_w\rangle$ vs wavelength λ_x. Again, it should be mentioned here that since only the turbulent contribution portion is considered, Cum_{turb} will not attain the value 100 % but C_{f2}/C_f at the largest wavelength.

Inner- and outer-scale normalized wavelengths are used in figures 7(*a*) and 7(*b*), respectively. As can be seen from figure 7(*a*), when the curves are represented as a function of inner-scale normalized wavelength λ_x^+, an obvious Reynolds number dependence of the curves can be observed, where the cumulative contribution value at a given λ_x^+ decreases as the Reynolds number increases. When the curves are represented as a function of outer-scale normalized wavelength λ_x/h (see figure 7*b*), though a minor Reynolds number dependence can still be observed, the curves at different Reynolds numbers generally agree well with each other.

By specifying appropriate cut-off wavelength ranges in figure 7, the contributions from specified scale range can be obtained. Motivated by the significant roles of VLSMs in contributing to the turbulent kinetic energy and Reynolds shear stress (carrying over 50 % of the kinetic energy and Reynolds shear stress (Guala *et al.* 2006; Balakumar & Adrian 2007; Duan *et al.* 2020*a*), we first adopted the most classical dividing wavelength $\lambda_x = 3h$ between LSMs and VLSMs to see the fractions of $\langle\tau_w\rangle$ contributed by VLSMs. Such results are presented in figures 8(*a*) and 8(*b*), where the results of present OCFs are shown in figure 8(*a*), and comparisons between OCF and CCF at $Re_\tau = 550$ (i.e. OCFDNS550 and CCFDNS550VL) are presented in figure 8(*b*). For the sake of completeness, the

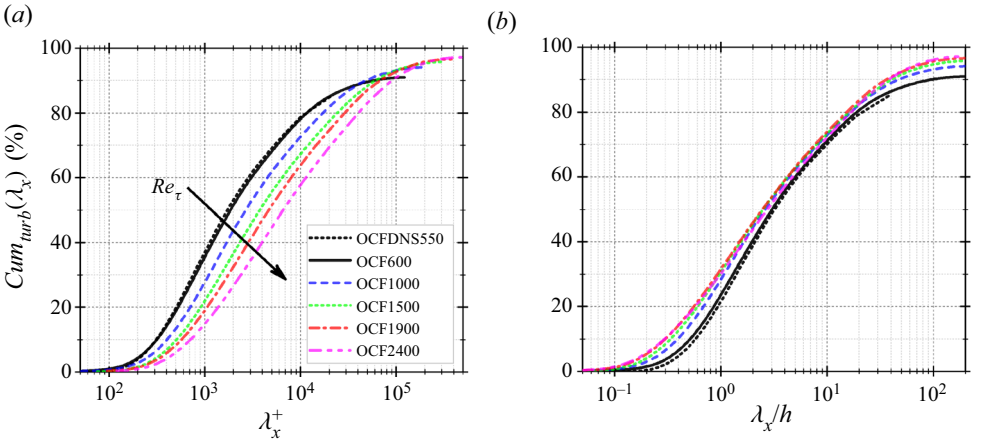

Figure 7. Cumulative turbulent contribution of physical length scales to $\langle\tau_w\rangle$, $Cum_{turb}(\lambda_x)$, where inner- and outer-scale normalized wavelengths are used in (*a*) and (*b*), respectively.

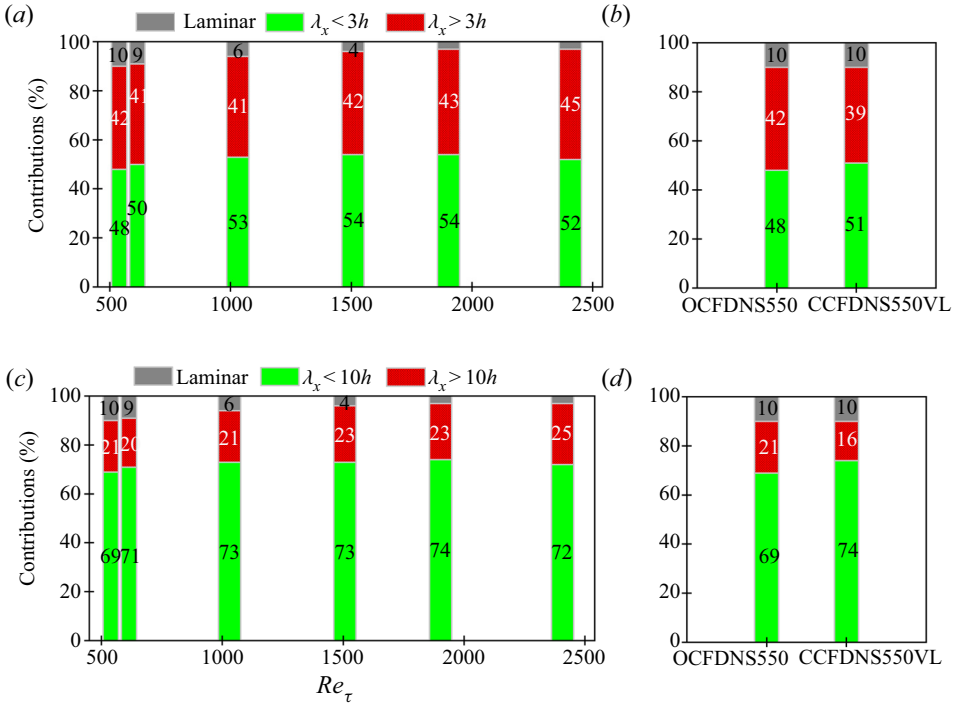

Figure 8. Contributions of different scale ranges of turbulent motions to $\langle\tau_w\rangle$ by adopting cut-off wavelengths of $\lambda_x = 3h$ (*a*,*b*) and $10h$ (*c*,*d*). (*a*,*c*) Results of present OCF cases at different Reynolds numbers. (*b*,*d*) Comparisons between OCF and CCF at $Re_\tau = 550$.

remaining contribution components (the laminar contribution, and contribution from $\lambda_x < 3h$) are also included. It can be seen that the VLSMs (with a wavelength $\lambda_x > 3h$) contribute over 40 %, while the turbulent motions with wavelength $\lambda_x < 3h$ contribute about 50 % of $\langle\tau_w\rangle$ in OCFs. Compared to CCF, slightly higher and lower contribution

values in $\lambda_x > 3h$ and $<3h$ range are observed in OCF (see figure 8*b*), which is expected according to the observations in the previous subsection.

Further results are obtained by adopting a larger dividing wavelength of $\lambda_x = 10h$ (approximately corresponding to the dividing wavelength that OCF and CCF exhibit differences in the turbulent contributions to $\langle\tau_w\rangle$, see figure 4), and the results are presented in figures 8(*c*) and 8(*d*). As can be seen in figure 8(*c*), the turbulent motions with $\lambda_x > 10h$ contribute over 20 % of $\langle\tau_w\rangle$, while the turbulent motions with $\lambda_x < 10h$ make a contribution of about 70 % in the present OCFs. The differences in the contributions from different scale ranges between OCF and CCF are again revealed in figure 8(*d*).

Finally, it is worth mentioning here that although the application of Taylor's hypothesis in the experimental cases (OCF1000 to OCF2400) would exert some effects on the curve shapes of Cum_{turb} in figure 7 and thus affect the exact contribution values in different scale ranges as shown in figure 8, such effects would not affect the main findings in figure 8 that turbulent motions with $\lambda_x > 3h$ contribute over 40 % of $\langle\tau_w\rangle$, and turbulent motions with $\lambda_x > 10h$ contribute over 20 % of $\langle\tau_w\rangle$. This statement is mainly supported by the OCFDNS550 case combined with the Reynolds number dependence trends, i.e. the contribution values (40 % for $\lambda_x > 3h$ and 20 % for $\lambda_x > 10h$) obtained in OCFDNS550 case are the lower bounds given that the contributions of these large scale turbulent motions to $\langle\tau_w\rangle$ increase as the Reynolds number increases. Therefore, it is safe to conclude here that the VLSMs with $\lambda_x > 3h$ contribute over 40 % of $\langle\tau_w\rangle$, and turbulent motions with $\lambda_x > 10h$ contribute over 20 % of $\langle\tau_w\rangle$ in OCFs within the Reynolds number range considered here (Re_τ from a low of 550 to a moderate value of 2400).

4. Conclusions

Contributions of different scales of turbulent motions to the mean wall-shear stress $\langle\tau_w\rangle$ in OCFs were quantified based on the FIK identity decomposition method combined with a scale decomposition. The OCF datasets considered herein covered both DNS and PIV experimental cases with the friction Reynolds number Re_τ ranging from a low of 550 to a moderate value of 2400. Comparisons of the results between OCF and CCF were also performed to reveal potential differences between the two flow configurations. The main findings can be summarized as follows.

(1) Both the 'laminar' and 'turbulent' components of $\langle\tau_w\rangle$ in OCFs have been shown to be identical to those in CCFs at identical Reynolds numbers, demonstrating the commonality of the two flow types.

(2) The scale-decomposed 'turbulent' contribution shows two dominant contribution modes (corresponding to LSMs and VLSMs) at a streamwise wavelength of $\lambda_x = 1 \sim 2h$ and $O(10h)$. As the Reynolds number increases, the contributions from the two modes (LSMs and VLSMs) gradually decrease and increase respectively, indicating the enhanced significance of VLSMs in contributing to $\langle\tau_w\rangle$ at higher Reynolds numbers. Within the Reynolds number range considered, the VLSMs with $\lambda_x > 3h$ account for over 40 % of $\langle\tau_w\rangle$ and turbulent motions with $\lambda_x > 10h$ account for over 20 % of $\langle\tau_w\rangle$.

(3) Comparisons of the scale-decomposed 'turbulent' contribution between OCF and CCF have revealed scale-dependent differences. Compared to CCFs, higher and lower contributions in $\lambda_x > O(10h)$ and $\lambda_x < O(10h)$ wavelength ranges are observed in OCFs. Given that the only difference between the two flows is the outer boundary, i.e. a free surface exists in OCFs, the above differences indicate important free surface effects on the turbulent contributions to $\langle\tau_w\rangle$ in OCFs.

Acknowledgements. We express our sincere gratitude to: Professor D.H. Richter (University of Notre Dame) for sharing the OCF DNS data at $Re_\tau = 550$; Dr R. Deshpande, Professor J.P. Monty, and I. Marusic (University of Melbourne) for sharing the CCF experimental data at $Re_\tau = 1000$; Dr A. Lozano-Durán (Stanford University) and Professor J. Jiménez (Universidad Politécnica Madrid) for sharing the very large domain size CCF DNS data at $Re_\tau = 550$; Professor M. Lee and R.D. Moser (The University of Texas at Austin) for making the CCF DNS database publicly available.

Funding. The study was financially supported by the National Natural Science Foundation of China (grant nos 51879138 and 51809268) and the Joint Fund of State Key Lab of Hydroscience and Institute of Internet of Waters Tsinghua-Ningxia Yinchuan (grant no. sklhse-2020-Iow06).

Declaration of interests. The authors report no conflict of interest.

Author ORCIDs.
Yanchong Duan https://orcid.org/0000-0003-0368-3620;
Qiang Zhong https://orcid.org/0000-0002-3171-9400;
Guiquan Wang https://orcid.org/0000-0003-4753-7676.

Appendix A. Data accuracy verification

A.1. *Statistical quantities*

Typical turbulent statistical quantities for present OCF cases are first presented in figure 9 to give a preliminary data accuracy verification. For comparison, the results of comparable CCF cases and theoretical formulas (e.g. log law for mean streamwise velocity, linear distribution of Reynolds shear stress in the outer region, and empirical functions for turbulence intensities proposed by Nezu & Rodi 1986) are also included. As seen in figure 9, there exists good agreement in the distribution of all turbulent quantities. The discrepancy in turbulence intensity between OCF and CCF in the nearly free surface region demonstrates the well-documented unique features of turbulent kinetic energy (TKE) redistribution in OCFs, i.e. the free surface dampens the wall-normal turbulence intensity but strengthens the wall-parallel ones.

A.2. *The uv cospectra and uncertainties*

Since the uv cospectrum Φ_{uv} is most essential to the scale decomposition of the mean wall-shear stress, its estimation method and accuracy should also be discussed herein. For the OCF DNS case (OCFDNS550), Φ_{uv} at a given y position was directly obtained from the spatial velocity data according to (2.2), among which the ensemble average was performed over spanwise positions and snapshots. For the experimental OCF flow cases, Φ_{uv} was obtained from the temporal velocity data using Welch's overlapped segment averaging method. The segment length was chosen to be long enough to ensure the largest wavelength resolved at all y positions is over $100h$. A segment overlap percentage of 50 % was adopted, based on which the segment number N_{seg} for the five cases (OCF600 to OCF2400) is $122 \sim 204$. To avoid spectral leakage at the segment edge, a hamming window was applied on each segment before performing the Fourier transform as advocated by Buxton, de Kat & Ganapathisubramani (2013). Given that the raw spectrum obtained from the raw velocity data would be inherently contaminated by the high-frequency measurement noise, a 9-point Gaussian kernel with a standard deviation of 1.7 was applied to the raw velocity data to reduce noise effects. And a bandwidth moving filter (BMF) (Baars *et al.* 2016) of 25 % (meaning that the filtered spectrum at wavenumber k_{xi} equals an average of the raw spectrum over a span of $k_{xi} \pm 25\,\%$) was further adopted to smooth the spectrum. One of main concerns on the experimental spectra is the use

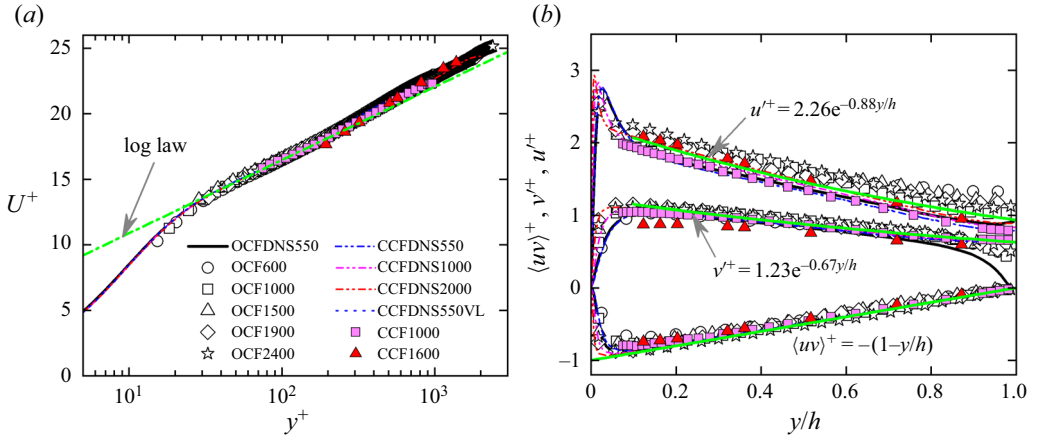

Figure 9. Wall-normal profiles of inner-scale normalized statistical quantities: (*a*) mean streamwise velocity; (*b*) turbulence intensities and Reynolds shear stress (here negative valued Reynolds shear stress is shown for a better demonstration purpose). The black line and symbols are present open channel flow (OCF) cases, and the remaining lines and symbols in color are these of closed channel flows (CCFs) and empirical functions for comparison. For the log law in (*a*), von Kármán constant $\kappa = 0.412$ and additive constant $A = 5.29$ are used (Nezu & Nakagawa 1993). The green lines and expressions in (*b*) indicate the classical functions for given quantities, among which the functions for the turbulence intensities are from Nezu & Rodi (1986).

of Taylor's hypothesis for frequency f to wavenumber k_x transformation: $k_x = 2\pi f/U_c$. As the only parameter in Taylor's hypothesis, the convection velocity U_c should depend on the localized motion scales and events (del Álamo & Jiménez 2009; de Kat & Ganapathisubramani 2015; Renard & Deck 2015; Fiscaletti, de Kat & Ganapathisubramani 2018) in theory, but complete expression of U_c with them is generally inaccessible in applications, given which a scale- and event-independent convection velocity is typically adopted for application purpose. Actually, in most cases where Taylor's hypothesis has been applied (e.g. the widely used single point HWA measurements in abundant studies, including the CCF1000 (Deshpande *et al.* 2020) and CCF1600 (Balakumar 2005; Balakumar & Adrian 2007) experimental cases considered herein), the local mean velocity U was the only accessible choice. Abundant studies have demonstrated that U is a good surrogate of U_c that could give sufficient accurate spectra results, except in the near-wall region (de Kat & Ganapathisubramani 2015; Squire *et al.* 2017, to name a few). In this study, for the convenience of comparison between the experimental OCF and CCF cases, we would mainly confine our estimations of the spectra through Taylor's hypothesis using the local mean velocity U. This would only exert minor effects on the main findings of this study, which has been discussed in § 3.

Figure 10 presents the resultant cospectra at a typical position ($y/h = 0.2$) to give a primary accuracy verification. The results of CCF cases at identical positions are also included for comparison. The high-frequency measurement noise can be readily seen at high wavenumber range of the raw unfiltered spectrum. The filtering procedures adopted herein effectively reduced this high-frequency noise and also the inherent fluctuations of the raw spectrum. A conservative estimation of the smallest scales that can be resolved at this position is $\lambda_x = 0.16h$ and $0.07h$, or equivalently $\lambda_x^+ = 100$ and 170, for the lowest and highest Re_τ, respectively. Good agreements observed between experiments and DNS, as well as between OCF and CCF cases, lend supports for the data accuracy and the rationality of processing procedures.

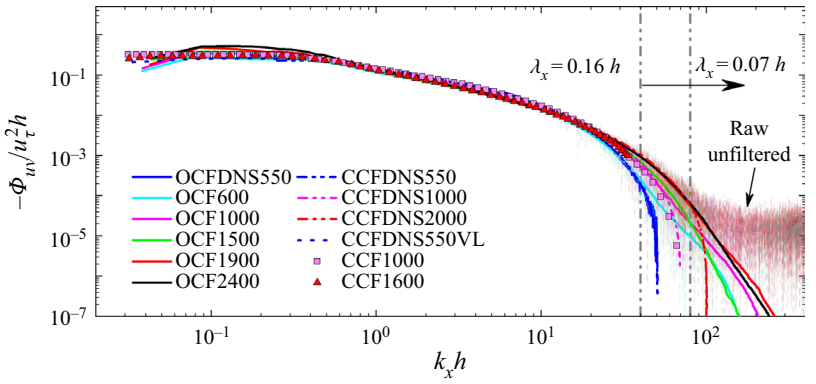

Figure 10. The uv cospectra Φ_{uv} at $y/h = 0.2$. The solid lines are present OCF results, among which the experimental ones are obtained from the Gaussian filtered velocity data followed by 25 % BMF filtering. As references, the raw unfiltered results obtained from the raw velocity data are also presented (as marked by an arrow in the figure). For comparison, the results of CCF cases at identical positions are also included.

Finally, the cospectra uncertainty will be briefly presented. Treating the spectrum estimation from each segment as a random quantity denoted as ϕ_{uv} whose ensemble average is the cospectra Φ_{uv}, the uncertainty of Φ_{uv} can be quantified according to the general uncertainty quantification method (Sciacchitano & Wieneke 2016) as $\delta\Phi_{uv} = \sigma_{\phi_{uv}}/\sqrt{N_{eff}}$. Here $\sigma_{\phi_{uv}}$ is the standard deviation of ϕ_{uv} and N_{eff} is the effective number of independent samples and can be replaced with the segment number N_{seg} herein. The uncertainty of DNS cases is generally expected to be negligible. Here we would put our emphasis on the experimental cases, for which $\delta\Phi_{uv}$ is estimated to be mainly at a level of $\sim$10 % Φ_{uv}, except in the near free surface region where Φ_{uv} is tending to zero (because $\langle uv \rangle$ is approaching zero therein) and for which reason the uncertainty $\delta\Phi_{uv}$ expressed as a percentage of Φ_{uv} would be higher.

References

Adrian, R.J. & Marusic, I. 2012 Coherent structures in flow over hydraulic engineering surfaces. *J. Hydraul Res.* **50** (5), 451–464.

Agostini, L. & Leschziner, M. 2019 The connection between the spectrum of turbulent scales and the skin-friction statistics in channel flow at $Re_\tau \approx 1000$. *J. Fluid Mech.* **871**, 22–51.

del Álamo, J.C. & Jiménez, J. 2009 Estimation of turbulent convection velocities and corrections to Taylor's approximation. *J. Fluid Mech.* **640**, 5–26.

Baars, W.J., Hutchins, N. & Marusic, I. 2016 Spectral stochastic estimation of high-Reynolds-number wall-bounded turbulence for a refined inner-outer interaction model. *Phys. Rev. Fluids* **1**, 054406.

Baars, W.J., Hutchins, N. & Marusic, I. 2017 Self-similarity of wall-attached turbulence in boundary layers. *J. Fluid Mech.* **823**, R2.

Baidya, R., Philip, J., Hutchins, N., Monty, J.P. & Marusic, I. 2017 Distance-from-the-wall scaling of turbulent motions in wall-bounded flows. *Phys. Fluids* **29**, 020712.

Balakumar, B.J. 2005 Nature of turbulence in wall-bounded flows. PhD thesis, University of Illinois at Urbana-Champaign, IL.

Balakumar, B.J. & Adrian, R.J. 2007 Large- and very-large-scale motions in channel and boundary-layer flows. *Phil. Trans. R. Soc. Lond.* A **365**, 665–681.

Bannier, A., Garnier, É. & Sagaut, P. 2015 Riblet flow model based on an extended FIK identity. *Flow Turbul. Combust.* **95**, 351–376.

Bauer, C. 2015 Direct numerical simulation of turbulent open channel flow. Master's thesis, Karlsruhe Institute of Technology.

Buxton, O.R.H., de Kat, R. & Ganapathisubramani, B. 2013 The convection of large and intermediate scale fluctuations in a turbulent mixing layer. *Phys. Fluids* **25**, 125105.

CAMERON, S.M., NIKORA, V.I. & STEWART, M.T. 2017 Very-large-scale motions in rough-bed open-channel flow. *J. Fluid Mech.* **814**, 416–429.

CHENG, C., LI, W.P., LOZANO-DURÁN, A. & LIU, H. 2019 Identity of attached eddies in turbulent channel flows with bidimensional empirical mode decomposition. *J. Fluid Mech.* **870**, 1037–1071.

CIERPKA, C., ROSSI, M. & KÖHLER, C.J. 2015 Wall shear stress measurements. In *Encyclopedia of Microfluidics and Nanofluidics*, 2nd edn (ed. D.Q. Li), pp. 3479–3486. Springer.

DECK, S., RENARD, N., LARAUFIE, R. & WEISS, P. 2014 Large-scale contribution to mean wall shear stress in high-Reynolds-number flat-plate boundary layers up to $Re_\theta = 13650$. *J. Fluid Mech.* **743**, 202–248.

DESHPANDE, R., MONTY, J.P. & MARUSIC, I. 2020 A scheme to correct the influence of calibration misalignment for cross-wire probes in turbulent shear flows. *Exp. Fluids* **61**, 85.

DUAN, Y.C., CHEN, Q.G., LI, D.X. & ZHONG, Q. 2020*a* Contributions of very large-scale motions to turbulence statistics in open channel flows. *J. Fluid Mech.* **892**, A3.

DUAN, Y.C., ZHANG, P., ZHONG, Q., ZHU, D.J. & LI, D.X. 2020*b* Characteristics of wall-attached motions in open channel flows. *Phys. Fluids* **32**, 055110.

FAN, Y.T., CHENG, C. & LI, W.P. 2019*a* Effects of the Reynolds number on the mean skin friction decomposition in turbulent channel flows. *Z. Angew. Math. Mech.* **40** (3), 331–342.

FAN, Y.T., LI, W.P. & PIROZZOLI, S. 2019*b* Decomposition of the mean friction drag in zero-pressure-gradient turbulent boundary layers. *Phys. Fluids* **31**, 086105.

FISCALETTI, D., DE KAT, R. & GANAPATHISUBRAMANI, B. 2018 Spatial-spectral characteristics of momentum transport in a turbulent boundary layer. *J. Fluid Mech.* **836**, 599–634.

FUKAGATA, K., IWAMOTO, K. & KASAGI, N. 2002 Contribution of Reynolds stress distribution to the skin friction in wall-bounded flows. *Phys. Fluids* **14** (11), L73–L76.

GAD-EL-HAK, M. 1994 Interactive control of turbulent boundary layers: a futuristic overview. *AIAA J.* **32** (9), 1753–1765.

DE GIOVANETTI, M., HWANG, Y. & CHOI, H. 2016 Skin-friction generation by attached eddies in turbulent channel flow. *J. Fluid Mech.* **808**, 511–538.

GOMEZ, T., FLUTET, V. & SAGAUT, P. 2009 Contribution of Reynolds stress distribution to the skin friction in compressible turbulent channel flows. *Phys. Rev.* E **79**, 035301(R).

GUALA, M., HOMMEMA, S.E. & ADRIAN, R.J. 2006 Large-scale and very-large-scale motions in turbulent pipe flow. *J. Fluid Mech.* **554**, 521–542.

HARITONIDIS, J.H. 1989 The measurement of wall shear stress. In *Advances in Fluid Mechanics Measurements* (ed. M. Gad-el-Hak), chap. 6, pp. 229–261. Springer.

HU, R.F., YANG, X.I.A. & ZHENG, X.J. 2020 Wall-attached and wall-detached eddies in wall-bounded turbulent flows. *J. Fluid Mech.* **885**, A30.

HWANG, J. & SUNG, H.J. 2017 Influence of large-scale motions on the frictional drag in a turbulent boundary layer. *J. Fluid Mech.* **829**, 751–779.

IWAMOTO, K., FUKAGATA, K., KASAGI, N. & SUZUKI, Y. 2005 Friction drag reduction achievable by near-wall turbulence manipulation at high Reynolds numbers. *Phys. Fluids* **17**, 011702.

KAMETANI, Y. & FUKAGATA, K. 2011 Direct numerical simulation of spatially developing turbulent boundary layers with uniform blowing or suction. *J. Fluid Mech.* **681**, 154–172.

KAMETANI, Y., FUKAGATA, K., ÖRLÜ, R. & SCHLATTER, P. 2015 Effect of uniform blowing/suction in a turbulent boundary layer at moderate Reynolds number. *Intl J. Heat Fluid Flow* **55**, 132–142.

DE KAT, R. & GANAPATHISUBRAMANI, B. 2015 Frequency-wavenumber mapping in turbulent shear flows. *J. Fluid Mech.* **783**, 166–190.

KIM, J., HWANG, J., YOON, M., AHN, J. & SUNG, H.J. 2017 Influence of a large-eddy breakup device on the frictional drag in a turbulent boundary layer. *Phys. Fluids* **29**, 065103.

KIM, K.C. & ADRIAN, R.J. 1999 Very large-scale motion in the outer layer. *Phys. Fluids* **11** (2), 417–422.

KLEWICKI, J.C., SARIC, W.S., MARUSIC, I. & EATON, J.K. 2007 Wall-bounded flows. In *Springer Handbook of Experimental Fluid Mechanics* (ed. C. Tropea, A.L. Yarin & J.F. Foss), chap. 12, pp. 871–907. Springer.

KOMORI, S., NAGAOSA, R., MURAKAMI, Y., CHIBA, S., ISHII, K. & KUWAHARA, K. 1993 Direct numerical simulation of three-dimensional open-channel flow with zero-shear gas-liquid interface. *Phys. Fluids* **5** (1), 115–125.

KUWATA, Y. & KAWAGUCHI, Y. 2018 Statistical discussions on skin frictional drag of turbulence over randomly distributed semi-spheres. *Intl J. Adv. Engng Sci. Appl. Maths* **10** (4), 263–272.

LEE, M. & MOSER, R.D. 2015 Direct numerical simulation of turbulent channel flow up to $Re_\tau \approx 5200$. *J. Fluid Mech.* **774**, 395–415.

LEE, M. & MOSER, R.D. 2019 Spectral analysis of the budget equation in turbulent channel flows at high Reynolds number. *J. Fluid Mech.* **860**, 886–938.

LI, W.P., FAN, Y.T., MODESTI, D. & CHENG, C. 2019 Decomposition of the mean skin-friction drag in compressible turbulent channel flows. *J. Fluid Mech.* **875**, 101–123.

LOZANO-DURÁN, A. & JIMÉNEZ, J. 2014 Effect of the computational domain on direct simulations of turbulent channels up to $Re_\tau = 4200$. *Phys. Fluids* **26**, 011702.

MARUSIC, I. & MONTY, J.P. 2019 Attached eddy model of wall turbulence. *Annu. Rev. Fluid Mech.* **51**, 49–74.

MEHDI, F., JOHANSSON, T.G., WHITE, C.M. & NAUGHTON, J.W. 2014 On determining wall shear stress in spatially developing two-dimensional wall-bounded flows. *Exp. Fluids* **55**, 1656.

MEHDI, F. & WHITE, C.M. 2011 Integral form of the skin friction coefficient suitable for experimental data. *Exp. Fluids* **50**, 43–51.

MODESTI, D., PIROZZOLI, S., ORLANDI, P. & GRASSO, F. 2018 On the role of secondary motions in turbulent square duct flow. *J. Fluid Mech.* **847**, R1.

MONTY, J.P., HUTCHINS, N., NG, H.C.H., MARUSIC, I. & CHONG, M.S. 2009 A comparison of turbulent pipe, channel and boundary layer flows. *J. Fluid Mech.* **632**, 431–442.

NEZU, I. 2005 Open-channel flow turbulence and its research prospect in the 21st century. *J. Hydraul. Engng* **131** (4), 229–246.

NEZU, I. & NAKAGAWA, H. 1993 *Turbulence in Open-Channel Flows*. Balkema.

NEZU, I. & RODI, W. 1986 Open-channel flow measurements with a laser Doppler anemometer. *J. Hydraul. Engng* **112** (5), 335–355.

NIKORA, V.I., STOESSER, T., CAMERON, S.M., STEWART, M., PAPADOPOULOS, K., OURO, P., MCSHERRY, R., ZAMPIRON, A., MARUSIC, I. & FALCONER, R.A. 2019 Friction factor decomposition for rough-wall flows: theoretical background and application to open-channel flows. *J. Fluid Mech.* **872**, 626–664.

PEET, Y. & SAGAUT, P. 2009 Theoretical prediction of turbulent skin friction on geometrically complex surfaces. *Phys. Fluids* **21**, 105105.

PERUZZI, C., POGGI, D., RIDOLFI, L. & MANES, C. 2020 On the scaling of large-scale structures in smooth-bed turbulent open-channel flows. *J. Fluid Mech.* **889**, A1.

RATHAKRISHNAN, E. 2017 Measurement of wall shear stress. In *Instrumentation, Measurements, and Experiments in Fluids*, 2nd edn (ed. E. Rathakrishnan), chap. 10, pp. 471–479. CRC.

RENARD, N. & DECK, S. 2015 On the scale-dependent turbulent convection velocity in a spatially developing flat plate turbulent boundary layer at Reynolds number $Re_\theta = 13\,000$. *J. Fluid Mech.* **775**, 105–148.

RENARD, N. & DECK, S. 2016 A theoretical decomposition of mean skin friction generation into physical phenomena across the boundary layer. *J. Fluid Mech.* **790**, 339–367.

RENARD, N. & DECK, S. 2017 Towards a physical scale decomposition of mean skin friction generation in the turbulent boundary layer. In *Progress in Turbulence VII* (ed. R. Örlü, A. Talamelli, M. Oberlack & J. Peinke), pp. 59–65. Springer.

SCARANO, F. 2002 Iterative image deformation methods in PIV. *Meas. Sci. Technol.* **13**, R1–R19.

SCIACCHITANO, A. & WIENEKE, B. 2016 PIV uncertainty propagation. *Meas. Sci. Technol.* **27**, 084006.

SENTHIL, S., KITSIOS, V., SEKIMOTO, A., ATKINSON, C. & SORIA, J. 2020 Analysis of the factors contributing to the skin friction coefficient in adverse pressure gradient turbulent boundary layers and their variation with the pressure gradient. *Intl J. Heat Fluid Flow* **82**, 108531.

SQUIRE, D.T., HUTCHINS, N., MORRILL-WINTER, C., SCHULTZ, M.P., KLEWICKI, J.C. & MARUSIC, I. 2017 Applicability of Taylor's hypothesis in rough- and smooth-wall boundary layers. *J. Fluid Mech.* **812**, 398–417.

STROH, A., FROHNAPFEL, B., SCHLATTER, P. & HASEGAWA, Y. 2015 A comparison of opposition control in turbulent boundary layer and turbulent channel flow. *Phys. Fluids* **27**, 075101.

TOWNSEND, A.A. 1976 *The Structure of Turbulent Shear Flow*. Cambridge University Press.

VINUESA, R. & ÖRLÜ, R. 2017 Measurement of wall-shear stress. In *Experimental Aerodynamics*, 1st edn (ed. S. Discetti & A. Ianiro), chap. 12, pp. 393–428. CRC.

WALKER, J.M. 2014 The application of wall similarity techniques to determine wall shear velocity in smooth and rough wall turbulent boundary layers. *Trans. ASME J. Fluids Engng* **136**, 051204.

WANG, G. & RICHTER, D.H. 2019 Two mechanisms of modulation of very-large-scale motions by inertial particles in open channel flow. *J. Fluid Mech.* **868**, 538–559.

WINTER, K.G. 1979 An outline of the techniques available for the measurement of skin friction in turbulent boundary layers. *Prog. Aerosp. Sci.* **18**, 1–57.

YOON, M., AHN, J., HWANG, J. & SUNG, H.J. 2016 Contribution of velocity-vorticity correlations to the frictional drag in wall-bounded turbulent flows. *Phys. Fluids* **28**, 081702.

YOON, M., HWANG, J. & SUNG, H.J. 2018 Contribution of large-scale motions to the skin friction in a moderate adverse pressure gradient turbulent boundary layer. *J. Fluid Mech.* **848**, 288–311.

ZHANG, W.H., ZHANG, H.N., LI, J.F., YU, B. & LI, F.C. 2020 Comparison of turbulent drag reduction mechanisms of viscoelastic fluids based on the Fukagata–Iwamoto–Kasagi identity and the Renard–Deck identity. *Phys. Fluids* **32**, 013104.

ZHANG, Z., SONG, X.D., YE, S.R., WANG, Y.W., HUANG, C.G., AN, Y.R. & CHEN, Y.S. 2019 Application of deep learning method to Reynolds stress models of channel flow based on reduced-order modeling of DNS data. *J. Hydrodyn.* **31** (1), 58–65.

ZHONG, Q., CHEN, Q.G., WANG, H., LI, D.X. & WANG, X.K. 2016 Statistical analysis of turbulent super-streamwise vortices based on observations of streaky structures near the free surface in the smooth open channel flow. *Water Resour. Res.* **52** (5), 3563–3578.

ZHONG, Q., LI, D.X., CHEN, Q.G. & WANG, X.K. 2015 Coherent structures and their interactions in smooth open channel flows. *Environ. Fluid Mech.* **15**, 653–672.